

Vortex survival in 3D self-gravitating accretion discs

Min-Kai Lin¹ *, Arnaud Pierens^{2,3}

¹*Institute of Astronomy and Astrophysics, Academia Sinica, Taipei 10617, Taiwan*

²*Université de Bordeaux, Observatoire Aquitain des Sciences de l'Univers, BP89 33271 Floirac Cedex, France*

³*CNRS, Laboratoire d'Astrophysique de Bordeaux, BP89 33271 Floirac Cedex, France*

16 May 2018

ABSTRACT

Large-scale, dust-trapping vortices may account for observations of asymmetric protoplanetary discs. Disc vortices are also potential sites for accelerated planetesimal formation by concentrating dust grains. However, in 3D discs vortices are subject to destructive ‘elliptic instabilities’, which reduces their viability as dust traps. The survival of vortices in 3D accretion discs is thus an important issue to address. In this work, we perform shearing box simulations to show that disc self-gravity enhances the survival of 3D vortices, even when self-gravity is weak in the classic sense (e.g. with a Toomre $Q \simeq 5$). We find a 3D, self-gravitating vortex can grow on secular timescales in spite of the elliptic instability. The vortex aspect-ratio decreases as it strengthens, which feeds the elliptic instability. The result is a 3D vortex with a turbulent core that persists for $\sim 10^3$ orbits. We find when gravitational and hydrodynamic stresses become comparable, the vortex may undergo episodic bursts, which we interpret as interaction between elliptic and gravitational instabilities. We estimate the distribution of dust particles in self-gravitating, turbulent vortices. Our results suggest large-scale vortices in protoplanetary discs are more easily observed at large radii.

Key words: accretion, accretion discs, hydrodynamics, instabilities, methods: numerical, protoplanetary discs

1 INTRODUCTION

Vortex dynamics is playing an increasingly important role in protoplanetary discs from both observational and theoretical perspectives. Several observations of transition discs reveal lopsided asymmetries in dust (van der Marel et al. 2013, 2016; Isella et al. 2013; Casassus et al. 2013; Fukagawa et al. 2013; Pérez et al. 2014; Hashimoto et al. 2015; Marino et al. 2015; Ohta et al. 2016; Kraus et al. 2017). Disc vortices provide a possible explanation because they are associated with localized pressure bumps, which can act as dust-traps (Barge & Sommeria 1995; Lyra & Lin 2013; Zhu et al. 2014). This interpretation suggests that large-scale vortices may be common in real protoplanetary discs.

The origin of protoplanetary disc vortices is usually attributed to hydrodynamic instabilities. To date, these include: the Rossby Wave Instability (RWI, Lovelace et al. 1999; Li et al. 2000; Meheut et al. 2010; Lin 2012b; Yellin-Bergovoy et al. 2016; Ono et al. 2016); the Sub-critical Baroclinic Instability (SBI, Petersen et al. 2007; Lesur & Papaloizou 2010; Lyra & Klahr 2011; Raettig et al. 2013; Barge et al. 2016); the Convective Overstability (ConO, Klahr & Hubbard 2014; Lyra 2014; Latter 2016); the Verti-

cal Shear Instability (VSI, Nelson et al. 2013; Stoll & Kley 2014; Barker & Latter 2015; Lin & Youdin 2015; Richard et al. 2016); and the Zombie Vortex Instability (ZVI, Marcus et al. 2015; Umurhan et al. 2016b; Lesur & Latter 2016). A common outcome of these instabilities is vortex formation and/or amplification.

Which of these hydrodynamic instabilities operate depends on the disc structure and thermal state, but taken together they pertain to a wide range of protoplanetary disc conditions (Umurhan et al. 2016a). Since these mechanisms form or amplify vortices, we can expect vortices to be natural features of protoplanetary discs. These vortices may assist in planetesimal formation by concentrating dust particles (Inaba & Barge 2006; Meheut et al. 2012).

Given the relevance of protoplanetary disc vortices to planet formation, it is essential to understand how they evolve under realistic conditions. A well-known result is that in three-dimensional (3D) discs vortices can develop secondary instabilities that weaken or even destroy them (Lithwick 2009; Lesur & Papaloizou 2009; Chang & Oishi 2010; Raiton & Papaloizou 2014). This would strongly threaten their survival in protoplanetary discs. It is therefore necessary to model disc vortices in 3D and account for such ‘elliptic instabilities’ to obtain realistic vortex lifetimes.

Another effect that is often neglected in modeling proto-

* mklin@asiaa.sinica.edu.tw

planetary disc vortices is their self-gravity. Disc self-gravity is usually described by the Toomre parameter

$$Q = \frac{c_s \Omega}{\pi G \Sigma}, \quad (1)$$

where c_s is the sound-speed, Ω is the disc's rotation frequency, Σ is the surface density, and G is the gravitational constant. Traditionally, self-gravity is considered important when $Q \lesssim 1$, which is the formal criterion for gravitational instability in laminar, axisymmetric thin discs (Toomre 1964). This typically translates to rather large disc-to-star mass ratios, $M_d/M_* \gtrsim 0.1$. However, the condition for gravitational instability, and hence the importance of self-gravity, can be relaxed when additional physics are considered (Lin & Kratter 2016).

The effect of self-gravity on the equilibrium structure of a disc vortex was first investigated by Adams & Watkins (1995) assuming circular vortices. However, the shear in protoplanetary discs likely only permits elliptical vortices (Lesur & Papaloizou 2009). Self-gravity has also been included in studies of vortex formation and evolution via the RWI (Lyra et al. 2009b; Lin & Papaloizou 2011a; Yellin-Bergovoy et al. 2016; Regály & Vorobyov 2017) and in gravito-turbulent discs (Mamatsashvili & Rice 2009).

In the case of the RWI, recent studies show that disc self-gravity affects vortex evolution when $Q \lesssim \pi/2h$ (Lovelace & Hohlfield 2013; Zhu & Baruteau 2016), where h is the disc aspect-ratio. For typical protoplanetary discs with $h \sim 0.05$, this means that self-gravity should be accounted when $Q \lesssim 20$; significantly larger than the classic condition. However, these calculations have been limited to razor-thin, two-dimensional (2D) discs.

The above discussion motivates us to study the evolution of elliptic vortices in 3D self-gravitating protoplanetary discs. This was first attempted by Lin (2012a) in global 3D numerical simulations of vortex formation via the RWI at planet gaps in self-gravitating discs. However, these simulations lacked the numerical resolution needed to capture the elliptic instability. Thus the survival of 3D vortices in self-gravitating discs remain unclear.

In this work, we study the evolution of 3D vortices in a local patch of a self-gravitating protoplanetary disc. We use the shearing box framework and insert a vortex to evolve as an initial value problem. While less realistic than Lin (2012a) in terms of vortex formation, this approach permits clean numerical experiments and higher resolution.

We find self-gravity enhances the survival of 3D vortices against the elliptic instability. The elliptic instability develops regardless of the strength of self-gravity, but with sufficient self-gravity the vortex subsequently undergoes a slow growth, with increasing levels of internal hydrodynamic turbulence. The vortex then undergoes bursts; alternating between coherent and turbulent cores. We interpret this as 'gravito-elliptic' feedback: a growing vortex spins up and develops hydrodynamic turbulence because of the elliptic instability, which contributes to further collapse by removing the large-scale internal rotation. The latter effect is similar to secular gravitational instabilities in viscous or dusty accretion discs (e.g. Youdin 2011; Takahashi & Inutsuka 2014; Lin & Kratter 2016).

This paper is organized as follows. We list the basic equations in §2. In §3 we give a qualitative discussion on

the expected effect of self-gravity on disc vortices. We describe our simulation setup and diagnostic measures in §4. We present simulation results in §5. We discuss implications of our simulations in §6 before summarizing in §7.

2 LOCAL DISC MODEL

We consider an inviscid, 3D self-gravitating accretion disc orbiting a central star. Cylindrical co-ordinates (R, ϕ, z) are centred on the star. The equilibrium rotation profile is described by $\Omega(R) \propto R^{-q}$. We are interested in Keplerian discs with $q = 3/2$ and vertical oscillation frequency $\Omega_z = \Omega$. We adopt the shearing box framework to study a small patch of the disc (Goldreich & Lynden-Bell 1965). Local Cartesian co-ordinates (x, y, z) are anchored on a fiducial point $(R_0, \phi_0, 0)$ in the global disc co-rotating with the background flow, so $\phi_0 = \Omega_0 t$ where $\Omega_0 \equiv \Omega(R_0)$. For simplicity, we drop the subscript zero hereafter.

The Cartesian shearing box fluid equations are

$$\frac{\partial \rho}{\partial t} + \nabla \cdot (\rho \mathbf{v}) = 0, \quad (2)$$

$$\frac{\partial \mathbf{v}}{\partial t} + \mathbf{v} \cdot \nabla \mathbf{v} = -\frac{1}{\rho} \nabla p - \nabla \Phi - 2\Omega \hat{\mathbf{z}} \times \mathbf{v} + \Omega^2 (2qx, 0, -z), \quad (3)$$

$$\nabla^2 \Phi = 4\pi G \rho, \quad (4)$$

where ρ is the mass density, \mathbf{v} is the total fluid velocity in the box, p is the pressure and Φ is the gravitational potential of the gas. We adopt an isothermal equation of state so that

$$p = c_s^2 \rho, \quad (5)$$

where $c_s = H\Omega$ is the constant isothermal sound-speed, with H being the disc scale-height at the reference radius.

A simple, steady state equilibrium solution to the above equations describes a stratified, axisymmetric shear flow with $\mathbf{v} = -q\Omega x \hat{\mathbf{y}}$ and $\rho = \rho(z)$. In dimensionless variables $\hat{\rho} \equiv \rho/\rho_0$, where ρ_0 is the mid-plane density, and $Z \equiv z/H$, the density field satisfies

$$\frac{d^2 \ln \hat{\rho}}{dZ^2} + \frac{\hat{\rho}}{Q_{3D}} + 1 = 0, \quad (6)$$

where

$$Q_{3D} \equiv \frac{\Omega^2}{4\pi G \rho_0} \quad (7)$$

is a self-gravity parameter for 3D discs (Mamatsashvili & Rice 2010). The boundary conditions are $\hat{\rho}(0) = 1$ and $d\hat{\rho}/dz = 0$ at $z = 0$. In the non-self-gravitating limit, $Q_{3D} \rightarrow \infty$, we obtain the usual Gaussian solution, $\hat{\rho} = \exp(-Z^2/2)$.

However, for non-self-gravitating discs there exists another class of equilibrium flow solutions corresponding to a vortex, which we discuss below.

3 VORTEX SOLUTIONS AND THE QUALITATIVE EFFECT OF SELF-GRAVITY

In this section we discuss the effect of disc self-gravity on equilibrium flows that correspond to a vortex. To this, it is useful to work in co-ordinates that reflect such a flow

pattern. We thus adopt the non-orthogonal ‘elliptico-polar’ co-ordinates (s, φ, z) defined by

$$x = s \cos \varphi, \quad (8)$$

$$y = \chi s \sin \varphi, \quad (9)$$

where χ is a constant, and z remains unchanged (see, e.g. [Kerswell 1994](#), for further discussion of this co-ordinate system). Here, we take $\chi > 1$ so that the co-ordinate $s \in [0, \infty)$ corresponds to the semi-minor axis of a series of similar ellipses, and $\varphi \in [0, 2\pi]$ corresponds to the azimuthal position along a given ellipse. We also define the fluid velocity components v_s, v_φ such that

$$v_x \hat{\mathbf{x}} + v_y \hat{\mathbf{y}} \equiv v_s \mathbf{s} + v_\varphi \boldsymbol{\varphi}, \quad (10)$$

where

$$\mathbf{s} \equiv \cos \varphi \hat{\mathbf{x}} + \chi \sin \varphi \hat{\mathbf{y}}, \quad (11)$$

$$\boldsymbol{\varphi} \equiv -\sin \varphi \hat{\mathbf{x}} + \chi \cos \varphi \hat{\mathbf{y}}. \quad (12)$$

The shearing box equations in elliptico-polar co-ordinates are listed in [Appendix A](#).

3.1 The GNG vortex in the absence of self-gravity

[Goodman et al. \(1987\)](#) present exact vortex solutions to [Eq. 2–3](#) in the absence of self-gravity (by setting $G = \Phi = 0$). Here, we review this ‘GNG’ vortex in elliptico-polar co-ordinates.

The GNG vortex corresponds to a steady axisymmetric flow in elliptico-polar co-ordinates in vertical hydrostatic equilibrium, so that $\partial_t = \partial_\varphi = v_s = v_z = 0$ and $v_\varphi = v_\varphi(s)$. The momentum equations then read

$$0 = \frac{v_\varphi^2}{s} - \frac{1}{2} (\xi_- \cos 2\varphi + \xi_+) \frac{\partial \eta}{\partial s} + \Omega v_\varphi \chi (\xi_- \cos 2\varphi + \xi_+) + q \Omega^2 s (\cos 2\varphi + 1), \quad (13)$$

$$0 = \frac{\xi_-}{2} \sin 2\varphi \frac{\partial \eta}{\partial s} - \Omega \chi \xi_- v_\varphi \sin 2\varphi - q \Omega^2 s \sin 2\varphi,$$

$$0 = z \Omega^2 + \frac{\partial \eta}{\partial z}, \quad (14)$$

where $\xi_\pm = 1 \pm 1/\chi^2$, and

$$\eta \equiv c_s^2 \ln \rho \quad (15)$$

is the gas enthalpy.

Since $\partial_\varphi = 0$ by construction, the trigonometric coefficients in [Eq. 13–14](#) must vanish. Then we obtain the flow solution

$$v_\varphi(s) = -\Omega_v s \text{ with } \Omega_v = \sqrt{\frac{2q}{\chi^2 - 1}} \Omega. \quad (16)$$

We have chosen the sign for Ω_v so that the flow is anti-cyclonic ([Bodo et al. 2007](#)). The corresponding density distribution is given via

$$\ln \frac{\rho}{\rho_c} = -\frac{s^2}{2H_{\text{eff}}^2} - \frac{z^2}{2H^2}, \quad (17)$$

where ρ_c is the density at $s = z = 0$ and the characteristic horizontal size H_{eff} is

$$H_{\text{eff}} \equiv \frac{H}{F}, \quad (18)$$

with

$$F^2(\chi; q) \equiv \frac{2}{\xi_-} \left[\frac{\sqrt{2q(\chi^2 - 1)}}{\chi} - q \right]. \quad (19)$$

Note that, in a Keplerian disc, the requirement $F^2 > 0$ imply non-self-gravitating vortices only exist with aspect-ratios $\chi > 2$.

3.2 Effect of self-gravity on the GNG vortex density field

The GNG solution is not compatible with self-gravity because the trigonometric coefficients of the Poisson equation in elliptico-polar co-ordinates do not vanish (see [Eq. A6](#)). This is because the gravitational potential of an ellipsoidal density distribution does not have the same symmetry, except for $s \rightarrow 0$ ([Chandrasekhar 1969](#)).

In order to get a sense of the effect of self-gravity, let us consider the region about $s = 0$ (vortex centroid), and simplify further by neglecting vertical stratification, so $\partial_z = z = 0$. For this cylindrical problem, we assume the self-gravitational potential has the form

$$\Phi = \frac{1}{2} A s^2 + \text{const.}, \quad (20)$$

for small s , where A is a constant. [Eq. 20](#) is consistent with the Poisson equation near the origin provided that

$$A = \frac{\Omega^2}{Q_{3D} \xi_+}. \quad (21)$$

Including self-gravity in the momentum equations amounts to the replacement $\eta \rightarrow \eta + \Phi$. Then

$$\begin{aligned} \frac{\partial \ln \rho}{\partial s} &= -\frac{s}{H_{\text{eff}}^2} - \frac{1}{c_s^2} \frac{\partial \Phi}{\partial s} = -\frac{s}{H_{\text{eff}}^2} \left(1 + \frac{1}{Q_{3D} \xi_+ F^2} \right) \\ &\equiv -\frac{s}{H_{\text{eff,sg}}^2}, \end{aligned} \quad (22)$$

where we have inserted the above approximation for Φ . Writing $H_{\text{eff,sg}} = H/F_{\text{sg}}$, we have

$$F_{\text{sg}}^2(\chi, Q_{3D}; q) \equiv \frac{H^2}{H_{\text{eff,sg}}^2} = F^2 + \frac{1}{Q_{3D} \xi_+}. \quad (23)$$

Thus self-gravity reduces the characteristic vortex size by increasing F^2 to $F^2 + 1/Q_{3D} \xi_+$.

In [Fig. 1](#) we plot the characteristic vortex size $H_{\text{eff,sg}}$ as a function of the aspect-ratio and self-gravity. The characteristic vortex size is insensitive to its aspect-ratio for $\chi \gtrsim 4$. At fixed χ the vortex size is reduced by self-gravity, but this effect is small for elongated vortices. Notice the minimum allowed aspect-ratio [defined by $F_{\text{sg}}^2(\chi) = 0$] is reduced by self-gravity. We show this in [Fig. 2](#): as $Q_{3D} \rightarrow 0$ the minimum aspect-ratio tends to unity.

Our estimate above differs from [Adams & Watkins \(1995\)](#), who found that self-gravity increases the size of a circular vortex. By contrast, [Fig. 1–2](#) indicates self-gravity reduces the size of elliptic vortices; and that circular vortices are only allowed in strongly self-gravitating discs.

3.3 Effect of self-gravity on the GNG vortex vorticity field

In [Appendix B](#), we give a more careful discussion of the effect of self-gravity. There, we also consider how self-gravity

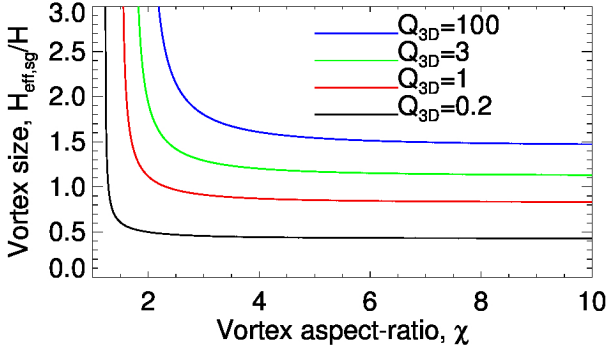


Figure 1. Characteristic horizontal vortex size, given by Eq. 23, as a function of the aspect-ratio, for a range of self-gravity parameters Q_{3D} .

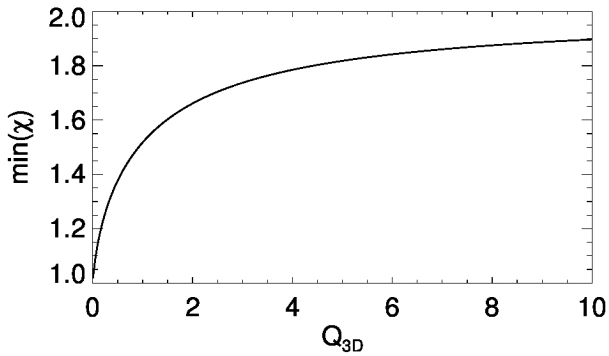


Figure 2. Minimum allowed aspect-ratio of the self-gravity-modified GNG vortex as a function of the self-gravity parameter Q_{3D} .

modifies the distribution of vertical vorticity of the GNG vortex. This effect is not obvious since potentials do not directly source vorticity.

We find the vorticity perturbation due to self-gravity is

$$\Delta\omega \propto (4\Omega_v - \Omega\chi\xi_+) \left(\frac{s}{H_{\text{eff}}} \right)^4 \quad (24)$$

near the vortex centre (see Eq. B37). For the GNG solution this implies that $\Delta\omega < 0$ for $\chi \gtrsim 2.5$. As we will be considering elongated vortices in practice, we expect that self-gravity enhances the GNG vortex by making its vorticity more negative. However, this is a small effect as the above estimate is restricted to $s \ll H_{\text{eff}}$. Adams & Watkins (1995) reached a similar conclusion for circular vortices, where they find self-gravity does not modify the vortex velocity field.

4 NUMERICAL SIMULATIONS

We simulate the evolution of a single vortex in the 3D, self-gravitating shearing box using the ATHENA code (Stone et al. 2008) to evolve Eq. 2–4. We adopt standard numerical configurations: third order reconstruction, a Roe solver, and Corner Transport Upwind (CTU) integrator. Disc self-gravity is solved via Fast Fourier Transform, but assuming a

vacuum beyond the vertical boundaries. We also use orbital advection (Stone & Gardiner 2010).

4.1 Grid setup and boundary conditions

The simulation domain is $x \in [-L_x, L_x]/2$, uniformly spaced with N_x grid points; and similarly for the y and z directions. Our fiducial box size and resolution is $(L_x, L_y, L_z) = (16H, 32H, 6H)$ with $(N_x, N_y, N_z) = (512, 512, 192)$, or 32 cells per H in the x, z directions and 16 cells per H in y . We use a lower resolution in the azimuth since we consider elongated vortices. The box size and numerical resolution is a compromise between having a sufficiently large box to minimize the influence of neighbouring vortices due to periodic boundary conditions (see below), and having enough resolution to capture the elliptic instability. We find this setup makes it feasible to simulate up to 2000 orbits. For selected cases we also double the x resolution.

We apply periodic boundary conditions in the y direction and shear-periodic boundary conditions in x . In the z direction we apply reflective boundary conditions for the momenta, and extrapolate the density field assuming vertical hydrostatic equilibrium. In addition, we apply damping for $|x| \in [0.8L_x, L_x]$ in which the hydrodynamic variables are relaxed towards their initial values on a timescale of 0.01 orbits. This is done to minimize spiral density waves launched by neighbouring vortices.

4.2 Units and self-gravity parameter

We adopt computational units such that $H = c_s = 1$, then $\Omega = 1$ as well. Time is quoted in units of the orbital period at the fiducial radius, $P_0 = 2\pi/\Omega$. The initial midplane density is $\rho_0 = 1$. In ATHENA, the strength of self-gravity is parameterized by the value of $4\pi G$. We specify it through $Q_{3D} = 1/4\pi G$ in computational units.

For the disc models considered in this work, the initial density distribution is approximately Gaussian, $\rho \simeq \rho_0 \exp(-z^2/2H^2)$. Then our self-gravity parameter Q_{3D} is related to the classic Toomre parameter Q by

$$Q_{3D} \simeq \sqrt{\frac{\pi}{8}} Q \quad (25)$$

Thus using Q or Q_{3D} is immaterial as they only differ by a factor of order unity. We will label our simulations with Q_{3D} , however, since this is the natural choice for 3D discs.

4.3 Initial condition and vortex perturbation

The GNG vortex described above is useful for analytic discussion due to its simple form, but is inconvenient to set as initial conditions in shearing box simulations because it is unbounded in the horizontal plane, which does not respect the standard shearing box boundary conditions. In a global disc, we expect the flow far from the vortex to return to orbital motion about the star.

We thus initialise an axisymmetric, 3D shearing box as described in §2 and apply the GNG vortex flow as a pertur-

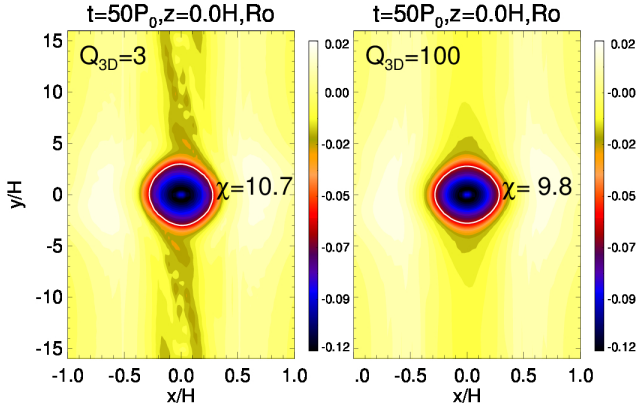


Figure 3. Vortex formed by perturbing the shearing box with the GNG vortex solution. Left: self-gravitating disc with $Q_{3D} = 3$. Right: effectively non-self-gravitating disc with $Q_{3D} = 100$. The colour scale corresponds to the Rossby number $Ro = (\nabla \times \mathbf{v})/2\Omega + q/2$

at the midplane. Here, χ is the aspect-ratio of the loci $Ro = 0.5\min(Ro)$ marked by the white contour.

bation:

$$\Delta v_x = \frac{\Omega_v}{\chi} y \exp(-m^2), \quad (26)$$

$$\Delta v_y = (q\Omega x - \Omega_v \chi x) \exp(-m^2), \quad (27)$$

with

$$m^2(x, y) \equiv \frac{x^2}{b^2} + \frac{y^2}{a^2} = \frac{1}{b^2} \left(x^2 + \frac{y^2}{\chi^2} \right), \quad (28)$$

where (a, b) is the semi-major and semi-minor axes of the vortex perturbation, respectively. Near the origin, the total velocity field is approximately that of the GNG vortex, while far from it one recovers the Keplerian shear flow.

We introduce the above velocity perturbations through source terms in the horizontal momentum equations over a timescale of $10P_0$. We specify the perturbation radial size b and aspect ratio χ , and obtain the appropriate value of Ω_v from Eq. 16. Fig. 3–4 shows that the initial vortex, formed by perturbing the disc with the GNG solution, is insensitive to Q_{3D} . The self-gravitating vortex is slightly more stratified (as found by Lin 2012a).

4.4 Diagnostics

Our key diagnostics are:

- The Rossby number

$$Ro \equiv \frac{\hat{z} \cdot \nabla \times \mathbf{v}}{2\Omega} + \frac{q}{2}, \quad (29)$$

as a dimensionless measure of the vertical vorticity relative to the background shear flow. The Rossby number can be used to measure the strength of the vortex, which can be defined as a coherent, extended region of $Ro < 0$ in the absence of turbulence (see Fig. 3).

- The vertical Mach number

$$M_z \equiv \frac{|v_z|}{c_s} \quad (30)$$

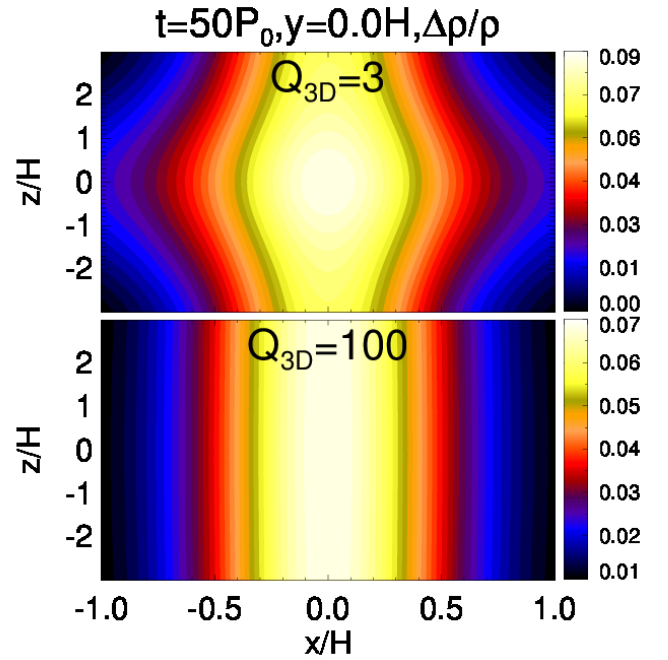


Figure 4. Vertical structure of vortices formed by perturbing the shearing box with the GNG vortex solution. Upper: self-gravitating disc with $Q_{3D} = 3$. Lower: non-self-gravitating disc with $Q_{3D} = 100$. The colour scale is the density perturbation relative to $t = 0$ (thus removing the background disc stratification).

to characterize vertical motions and thus the elliptic instability, which is expected to be three-dimensional (Lesur & Papaloizou 2009).

- The Reynolds and gravitational stresses

$$\alpha_R \equiv \frac{1}{c_s^2} v_x (v_y + q\Omega x), \quad (31)$$

$$\alpha_G \equiv \frac{1}{c_s^2} \frac{\partial_x \Phi \partial_y \Phi}{4\pi G \rho}, \quad (32)$$

to characterize turbulent activity. The total stress is $\alpha \equiv \alpha_R + \alpha_G$.

- Vortex characteristics. We calculate the evolution of the vortex shape in post-processing, as follows. For this we use the vortex density field because it remains smooth throughout the simulation. (The vorticity field can involve small-scale structures so it becomes difficult to define a large-scale coherent pattern.) We first locate the horizontal coordinates (x_v, y_v) of $\max(\rho)$ near the origin. We define the vortex boundary as the contour around (x_v, y_v) on which $\rho = 0.5\max(\rho)$. This contour is usually close to an ellipse, except at late evolution. We then define the semi-minor and major vortex axes, b_ρ and a_ρ , as half the length and width of the contour, respectively. The corresponding aspect ratio is $\chi_\rho = a_\rho/b_\rho$.

We define the density-weighted average value of a quantity f as

$$\langle f \rangle \equiv \frac{\int_V \rho f dV}{M_V}, \quad (33)$$

where

$$M_{\mathcal{V}} \equiv \int_{\mathcal{V}} \rho dV, \quad (34)$$

and the sample volume \mathcal{V} is $x \in [-b, b]$.

5 RESULTS

Table 1 summarizes the simulations we have carried out. Our fiducial set of runs, which are highlighted in bold and discussed in detail below, are Q3, Q4, Q5 and Q100. The initial vortex aspect-ratio is $\chi = 10$ with radial size $b = H/2$. Note that axisymmetric instability in 3D shearing boxes require $Q_{3D} \lesssim 0.2$ (Mamatsashvili & Rice 2010). Thus all cases are gravitationally stable in the absence of the vortex. (They correspond to Toomre parameters $Q \gtrsim 5$.)

5.1 Overview

Fig. 5 shows the evolution of average mass, Rossby number, vertical Mach number, and stresses in the sample volume $x \in [-b, b]$ and time-averaged over 5 orbits. Without self-gravity ($Q_{3D} = 100$) the vortex decays by $t \sim 700P_0$, after which vertical motions remain small ($|v_z| \sim 10^{-3}c_s$) and the average Rossby number roughly constant, as is $M_{\mathcal{V}}$. The box returns to a laminar state with $\alpha \sim 10^{-7}$.

By contrast, the self-gravitating cases with $3 \leq Q_{3D} \leq 5$ are characterized by an increase in $M_{\mathcal{V}}$ for $t \gtrsim 300P_0$ with a corresponding increase in $|\text{Ro}|$, $|v_z|$, and α . These indicate sustained 3D turbulence developed from the elliptic instability as the vortex spins up due to self-gravitational growth. The self-gravitating vortices survive longer than the non-self-gravitating case. However, the $Q_{3D} = 3$ vortex weakens again after becoming too strong ($t \gtrsim 1500P_0$, see §5.5).

Fig. 6 shows the evolution of the Toomre Q parameter measured at the vortex center, the density-based vortex semi-minor axis b_{ρ} and aspect-ratio χ_{ρ} . The Toomre parameter remains $Q > 2$, which would suggest self-gravity to be unimportant in the classic sense. Evidently this is not the case: we observe vortex growth even with a Toomre $Q \sim 8$ initially.

The vortex aspect-ratio first increases as the elliptic instability weakens the vortex. Without self-gravity the vortex eventually decays into a ring. For $Q_{3D} = 5$ the aspect-ratio is maintained at $\chi_{\rho} \sim 14$ –15. For $Q_{3D} = 3, 4$ the aspect ratio decreases, first slowly then rapidly from $t \sim 1200P_0, 1500P_0$ for $Q_{3D} = 3, 4$, respectively. Notice this drop coincides with when self-gravity becomes dominant with $\alpha_G > \alpha_R$.

Finally, in Fig. 7 we compare the stresses averaged over the simulation domain excluding buffer zones. These are qualitatively similar to stresses measured at the box centre, but the total stress is always dominated by the Reynolds contribution. This reflects the fact that all of the discs under consideration are weakly self-gravitating in the classic sense.

5.2 Elliptic instability

We find early vortex evolution and weakening ($t \lesssim 300P_0$) is driven by elliptic instability (EI) and independent of self-

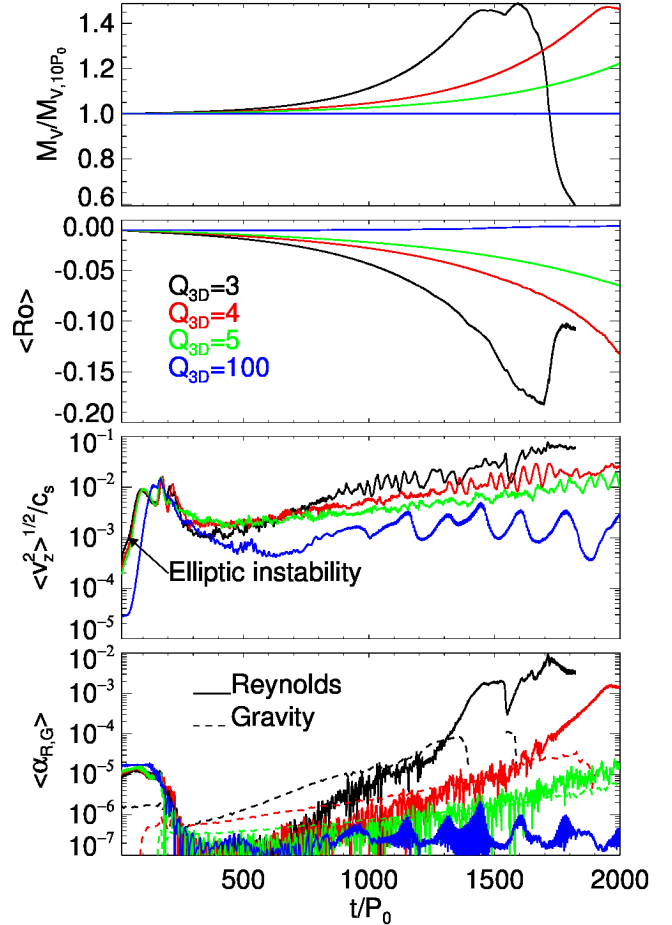


Figure 5. Top to bottom: total mass, Rossby number, vertical Mach number, and stresses measured in the sample volume $|x| \leq H/2$ containing the vortex for different strengths of self-gravity. These correspond to runs labeled Q3, Q4, Q5, and Q100 in Table 1.

gravity¹. The EI is signified by the exponential increase in $\sqrt{\langle v_z^2 \rangle}$ in $t \lesssim 100P_0$ with growth rate $\gamma \simeq 0.01\Omega$ and saturating at $\sqrt{\langle v_z^2 \rangle} \sim 0.01c_s$ in all cases. This is consistent with previous non-self-gravitating studies of the EI, and the weak dependence on self-gravity is expected since the EI is incompressible (Lesur & Papaloizou 2009). The left panels in Fig. 8 show the result of the EI is small-scale hydrodynamic turbulence. The subsequent evolution then depends on self-gravity.

5.3 Secular vortex growth and sustained turbulence

Fig. 8 compares the secular evolution of the vortex after the initial EI. In both self-gravitating and non-self-gravitating cases, the initial EI results in an irregular vorticity field ($t = 250P_0$). However, it then reorganises into a larger, coherent vortical structure by $t = 500P_0$, which serve as initial

¹ However, adjustment to the background Keplerian shear may also have minor contributions to the early vortex evolution.

Table 1. Summary of simulations. In all runs an initial phase ($t \lesssim 300P_0$) of elliptic instability weakens/lengthens the vortex. The subsequent evolution is described below. The fiducial runs are in bold and discussed in the text.

Run	Q_{3D}	z_{\max}	χ	N_x/L_x	Vortex evolution
Q100	100	$3H$	10	$32/H$	Vortex destroyed by initial EI and decays into an axisymmetric density bump.
Q100z2HR	100	$2H$	10	$64/H$	Vortex destroyed by the initial EI.
Q5	5	$3H$	10	$32/H$	Vortex survives until the end of the simulation ($t = 2000P_0$) with a turbulent core with 3D motions.
Q4	4	$3H$	10	$32/H$	Similar to Q5, but the vortex undergoes an azimuthal collapse from $t \sim 1500P_0$ when $\alpha_R \gtrsim \alpha_G$ in the vortex and oscillations in $ v_z $ develops. For $t \gtrsim 1700P_0$ $\max v_z $ appears outside the vortex core. An over-dense vortex remains at the end of the simulation.
Q4HR	4	$3H$	10	$64/H$	Vortex destroyed by the initial EI.
Q4z2HR	4	$2H$	10	$64/H$	Vortex survives with a turbulent core.
Q4c5	4	$3H$	5	$32/H$	Vortex destroyed by initial EI.
Q4c20	4	$3H$	20	$32/H$	Similar to Q4, but azimuthal collapse occurs sooner at $t \sim 1000P_0$.
Q3	3	$3H$	10	$32/H$	Similar to $Q_{3D} = 4$, but azimuthal collapse begins earlier ($t \sim 1200P_0$). Vertical motions dominates outside the vortex core from $t \sim 1400P_0$. Vortex decays after reaching a size of $b \sim H$ at $t \sim 1500P_0$ and inducing spiral shock waves in the ambient disc.
Q3HR	3	$3H$	10	$64/H$	Vortex survives with a turbulent core.
Q3z2HR	3	$2H$	10	$64/H$	Vortex survives with a turbulent core. (Simulation terminated at $t = 1200P_0$.)

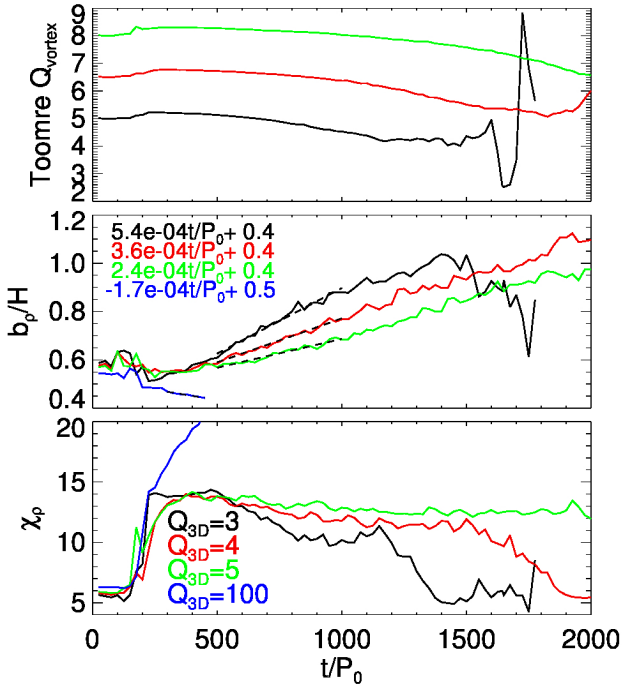


Figure 6. Time evolution of the Toomre Q parameter at the vortex centre (top), vortex semi-minor axis (middle) and aspect-ratio (bottom). Measurements are based on the vortex density field. For $Q_{3D} = 100$ the Toomre $Q \gtrsim 150$ and is therefore not shown. Dashed lines in the middle panel are linear fits to the growth in b_p .

conditions for secular evolution. This initial vortex ‘revival’ may be due to the Kelvin-Helmholtz instability of vorticity strips that result from the shearing of vorticity seeds by the background shear flow left by the initial EI (Lith-

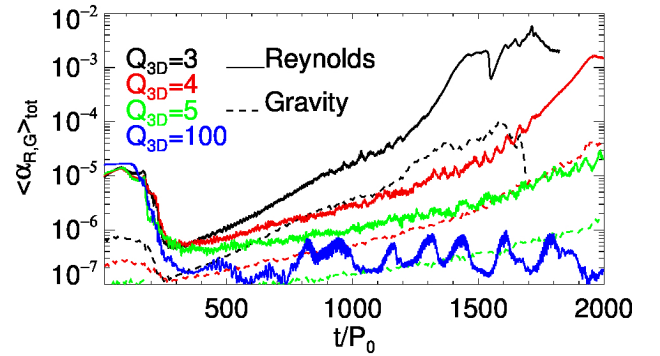


Figure 7. Stresses averaged over the simulation domain for the fiducial runs.

wick 2007). This second-generation vortex then undergoes EI again. However, in the non-self-gravitating case the vortex simply decays: we do not observe the reemergence of a large-scale coherent vortex due to Lithwick’s mechanism.

By contrast, we find that in self-gravitating discs the large-scale vortex persists with small-scale 3D hydrodynamic turbulence in its core (Fig. 8, upper panel). The vortex undergoes secular growth from $t \sim 300P_0$ to the end of the simulation for $Q_{3D} = 5$, but only to $t \sim 1500P_0$, $1200P_0$ for $Q_{3D} = 4$, 3 , respectively. (In the latter cases the vortex then undergoes an azimuthal collapse, see §5.5.) Stresses $\langle \alpha \rangle$ and vertical velocity fluctuations $\sqrt{\langle v_z^2 \rangle}$ grow exponentially, but with growth rate $\sim 2-9 \times 10^{-4}\Omega$, significantly slower than the initial EI because of the larger vortex aspect ratios than those imposed initially (Lesur & Papaloizou 2009). However, notice $\sqrt{\langle v_z^2 \rangle}$ grows faster with decreasing Q_{3D} . This indicates stronger EI, which is due to smaller vortex aspect-ratios with increasing self-gravity (see Fig. 6).

Fig. 9 shows the evolution of the density field during secular growth. The self-gravitating vortex increases in density

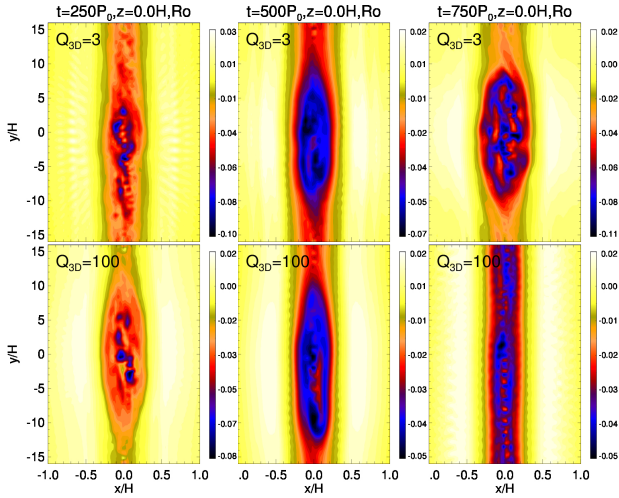


Figure 8. Hydrodynamic turbulence due to the elliptic instability of a 3D vortex in a self-gravitating disc (upper panels), and in a non-self-gravitating disc (lower panels). Comparing the upper and lower panels show that hydrodynamic turbulence can be sustained (and grows) in the presence of self-gravity. Colors show the Rossby number $Ro = (\nabla \times \mathbf{v}) / 2\Omega + q/2$ at $z = 0$.

and size, but with decreasing aspect-ratio. Notice the density field remains smooth even though the vorticity field is turbulent. This reflects the incompressible nature of the EI. By contrast, the non-self-gravitating vortex is destroyed by the initial EI, leaving an axisymmetric density ring.

We note that during secular growth the monotonic increase in the vortex mass, rotation, and semi-minor axis (Fig. 5–6) in the self-gravitating cases proceed more rapidly than the decrease in its aspect-ratio. (For $Q_{3D} = 5$ the vortex aspect-ratio is nearly constant.) A possible reason is that vertical stratification due to self-gravity (see Fig. 4) makes the secular dynamics more similar to that of 2D vortices (Umurhan & Regev 2004; Johnson & Gammie 2005; Shen et al. 2006). These studies show that 2D vortices tend to merge into larger vortices (Godon & Livio 1999). Though merging cannot occur for our single, isolated vortex; secular evolution towards larger scales can be expected if the system behaves two-dimensionally due to the inverse cascade of energy (Kraichnan & Montgomery 1980). However, the additional stratification brought about by self-gravity is small; thus this effect is unlikely important for the present Q_{3D} values. Here, the vortex growth in its radial size may be simply due to mass accretion.

5.4 Episodic bursts

We find secular vortex growth ends when $\alpha_R \sim \alpha_G \sim 10^{-5}$, at which point we observe *episodic bursts* of EI in self-gravitating cases. This is reflected in Fig. 5 as oscillations in $\sqrt{\langle v_z^2 \rangle}$, starting from $t \sim 1000P_0, 1500P_0$ for $Q_{3D} = 3, 4$, respectively; and it only just begins to develop at the end of the $Q_{3D} = 5$ simulation. Fig. 10 show snapshots of this episodic behaviour for $Q_{3D} = 4$ (where the simulation output frequency conveniently coincides with the burst.) The vortex oscillates between having small-scale turbulence ($t = 1575P_0, 1625P_0$) and a coherent patch of negative vor-

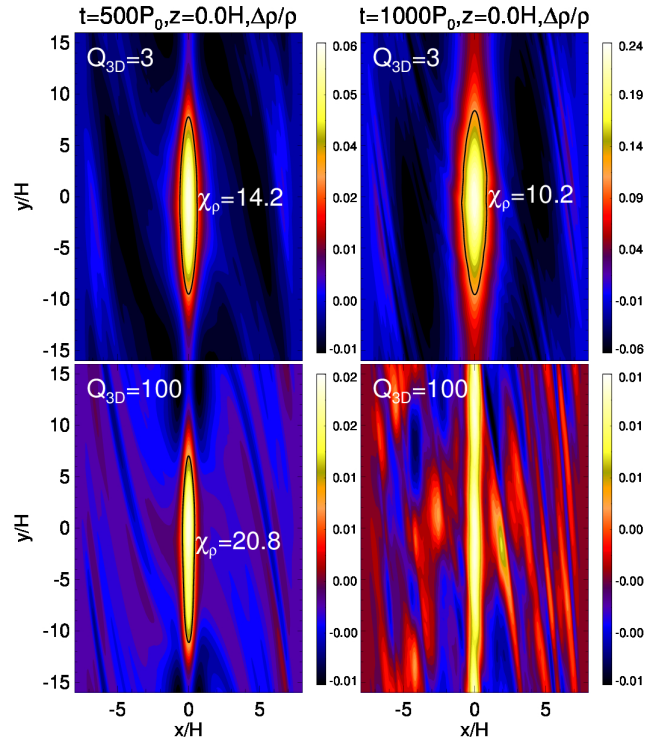


Figure 9. Secular vortex evolution, after the initial development of elliptic instability and corresponding hydrodynamic turbulence. Top: a self-gravitating disc. Bottom: non-self-gravitating disc. Colors show the relative density perturbation at the mid-plane.

ticity ($t = 1600P_0, 1650P_0$). Notice in that $\max |Ro|$ also oscillates.

We comment that the oscillations are not reflected by the Rossby number in Fig. 5 because Ro has been averaged over $x \in [-b, b]$, which demonstrates that overall the vortex continues to strengthen. Nevertheless, we checked that $|Ro|$ does oscillate during the burst phase when the sampling volume is limited to near the vortex centre.

This episodic behavior suggests competition between vortex growth due to self-gravity and vortex destruction by the EI. As the vortex grows, it spins up ($|Ro|$ increases) and its aspect-ratio decreases. This feeds the EI, which converts some of the vortex’s large-scale, planar rotation into small-scale 3D turbulence (signified by an increasing $|v_z|$). The EI activity decays, but is re-triggered once the vortex reforms as it grows via self-gravity. This growth may be partly attributable to the removal of the vortex’s internal rotation by the EI and enabling secular gravitational instabilities (see §6.2).

A similar bursty behaviour has been reported in 3D simulations of vortex amplification by the sub-critical baroclinic instability in competition with EI (Lesur & Papaloizou 2010, their Fig. 16). We discuss this analogy further in §6.3.

5.5 Azimuthal collapse, gap opening, and self-destruction

As Reynolds stresses (α_R) increases beyond the gravita-

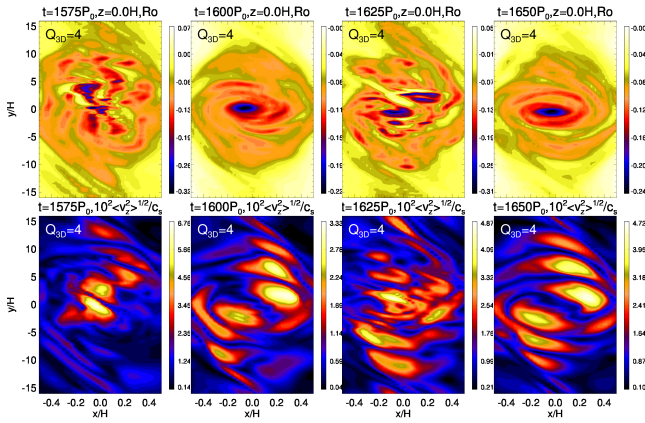


Figure 10. Example of episodic elliptic instability in a self-gravitating 3D vortex. Top: Rossby number. Bottom: vertical Mach number.

tional stresses (α_G), the vortex in the $Q_{3D} = 3, 4$ discs enter a second, faster collapse phase where its aspect-ratio rapidly drops, although its radial size continues to grow, see Fig. 5–6. This azimuthal collapse phase corresponds to $t \in [1200, 1500]P_0$ and $t \in [1500, 2000]P_0$ for $Q_{3D} = 3, 4$, respectively. The total stress also increases rapidly (see Fig. 7).

Fig. 11 shows azimuthal collapse for the $Q_{3D} = 3$ simulation. The vortex exits the bursty phase with a coherent vorticity patch of aspect-ratio $\chi \sim 7$ (upper middle panel). Notice $\max|v_z|$ moves outside the vortex core as its aspect-ratio decreases (lower right panel). This is in fact consistent with Lesur & Papaloizou (2009), who find the EI occurs outside the vortex core for an intermediate range of aspect-ratios in the absence of buoyancy, as is the case for isothermal gas considered here. In their specific case of Kida vortices (Kida 1981), this range is $4 \lesssim \chi \lesssim 6$, but the corresponding range may differ for the vortices in our simulations.

We find azimuthal collapse is associated with vortex-driven spiral density waves. Spiral density waves are naturally excited by vortex modes in compressible gas (Bodo et al. 2005; Heinemann & Papaloizou 2009; Mamatsashvili & Chagelishvili 2007). However, as the vortex half-width approaches H , these spiral density waves steepen into shocks (Paardekooper et al. 2010) and transfer angular momentum and energy away from the vortex (Bodo et al. 2007). These spiral shocks can also be identified visually in Fig. 11 at $t = 1500P_0$ in both the density and vorticity maps.

Azimuthal collapse is terminated once the vortex half-width exceeds $\sim H$. This is seen in Fig. 5 as the rapid drop in $|Ro|$ towards the end of the simulation with $Q_{3D} = 3$. The corresponding decrease in M_v indicate mass loss by the vortex to the ambient disc. This final vortex weakening is likely related to the strong spiral shocks induced by the vortex once it becomes too large in the radial direction. We observe a similar self-destruction behaviour as above in an extended run of the $Q_{3D} = 4$ case. However, a proper study of this final stage require global simulations to minimize the influence of radial boundary conditions. We thus limit our discussion here to when $b_p \lesssim H$. (See Appendix C for examples of vortex evolution in 2D, global discs.)

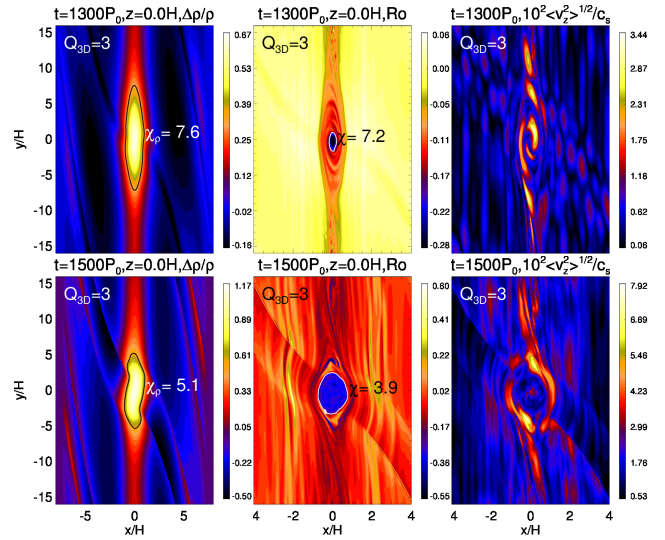


Figure 11. Evolution of the $Q_{3D} = 3$ vortex during azimuthal collapse, when its aspect-ratio drops rapidly. Left: midplane density perturbation. Middle: midplane Rossby number. Right: average vertical Mach number. Here, ellipses in Ro are drawn by inspection, and correspond to the loci $Ro = 0.65\min(Ro)$ and $Ro = 0.3\min(Ro)$ in the top and bottom snapshots, respectively.

Nevertheless, our observation that vortex radial size being limited by the associated density waves is consistent with previous studies of vortex evolution in 2D. The critical radial extent is expected to be $\sim H$ (Godon & Livio 1999), beyond which the vortex flow becomes sonic (Paardekooper et al. 2010). This is equivalent to the Jeans length $\lambda_J \sim O(QH)$ in a self-gravitating disc with $Q \sim 1$. Indeed, Mamatsashvili & Rice (2009) suggest 2D vortices are limited to λ_J in their radial extent. They find in gravito-turbulent discs that upon reaching λ_J , 2D vortices weaken and are sheared away by the background flow (Lyra et al. 2009b, see also). In our discs with $Q > 1$, λ_J is somewhat larger than H . The vortex width limit in our 3D simulations is thus similar to that in corresponding 2D, non-self-gravitating discs.

Notice in Fig. 11 that two shallow gaps have developed on either side of the vortex. Similar double-gap structures appear in low mass planet-disc simulations (e.g. Zhu et al. 2013; Dong et al. 2017). This suggests that the vortex can interact with the ambient disc in a similar way to disc-planet interaction. The strength of gravitational interaction between the vortex and the ambient disc can be estimated via the total mass M_{pert} enclosed in the elliptical patch ($x^2 + y^2/\chi_p^2$)/ $b_p^2 \lesssim 1$:

$$q_v \equiv \frac{M_{\text{pert}}}{M_* h^3} = \frac{\chi_p}{Q} \left(\frac{b_p}{H} \right)^2, \quad (35)$$

where M_* is the mass of the central star and $h \equiv H/R$ is the characteristic disc aspect-ratio at the fiducial radius of the shearing box. Using Fig. 6 we find $q_v \sim 1.3$ for the $Q_{3D} = 3$ simulation at $t = 1500P_0$. This can be compared to the thermal condition for gap-opening by disc-planet interaction, $q_v \gtrsim 1$ (Crida et al. 2006). Thus gap-opening by the vortex can be indeed be expected. However, we expect

gap-opening by an elliptical, extended vortex to be weaker than by a point-mass planet of the same mass.

The vortex-induced spiral shocks may also contribute to mass accretion onto the vortex, similar to shock-driven accretion in circumplanetary discs (Zhu et al. 2016). Both 1) the increasing vortex mass; and 2) the decreasing vortex aspect-ratio are expected to enhance the vortex-driven spiral density waves. Thus azimuthal collapse proceeds more rapidly than the secular growth, when the associated spiral waves are weak. Turbulence outside the vortex core may also contribute to angular momentum removal and hence mass accretion by the vortex.

5.6 Vortex aspect-ratio, numerical resolution, and box height

We performed several variations of the fiducial runs described above. These are summarized in Table 1 and include different aspect-ratios for the initial vortex perturbation (χ), the radial resolution (L_x/N_x), and the vertical domain size (z_{\max}),

For the $Q_{3D} = 4$ disc we ran additional cases with $\chi = 20$ and $\chi = 5$ for the initial vortex perturbation. The former behaves similarly to our fiducial run with $\chi = 10$. However, for $\chi = 5$ the vortex is destroyed by the initial phase of EI, similar to the non-self-gravitating case Q_{100} . This suggests that self-gravity cannot save vortices born with small aspect-ratios.

We also repeated some runs with twice the radial resolution. These are compared in Fig. 12 for the $Q_{3D} = 3$ disc. We find the initial EI growth rate is converged, but with better resolution the resulting turbulence leads to a weaker vortex to serve as initial conditions for secular growth. This is shown in Fig. 13 as the more elongated vortex at $t = 500P_0$ compared to that in Fig. 8. Since the EI turbulence is better resolved, it has a more destructive effect and the subsequent secular growth rate is slower and a 3D vortex with a turbulent core persists until the end of the simulation.

We find that reducing the vertical domain also enhances vortex survival, which is as expected as the system is forced to behave more two-dimensionally (Lithwick 2009). This is demonstrated in Fig. 14 with simulations using $Q_{3D} = 4$. Starting from the fiducial run with $z_{\max} = 3H$, we double the radial resolution and find the vortex is destroyed by the initial EI. (Comparing with Fig. 13 confirms that self-gravity enhances vortex survival.) However, retaining the same resolution but setting $z_{\max} = 2H$ results in a persistent 3D vortex with a turbulent core, also shown in Fig. 15.

These additional runs indicate that, in order to undergo self-gravitational growth, a 3D vortex needs to maintain its large-scale internal flow. Thus the initial EI cannot be too strong. This can be limited by diffusion (numerical in our case) and/or limited vertical domain. Notice in the simulations where a vortex persists that $\alpha_G > \alpha_R$ during secular growth, as observed in the standard run. We suggest this condition required for long-term vortex survival. If the initial EI-turbulence destroys the large-scale vortex topology, then there is no vortex for self-gravity to maintain or amplify.

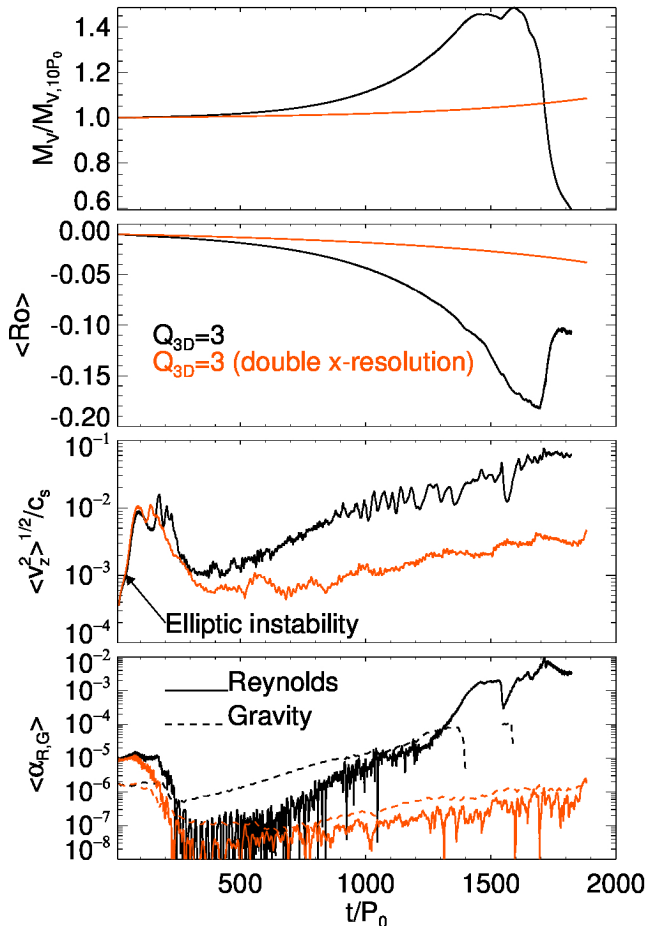


Figure 12. Comparison between vortex evolution in a $Q_{3D} = 3$ disc, but different radial resolutions: $N_x/L_x = 32/H$ (black) and $64/H$ (orange). The vortex persists in both simulations.

6 DISCUSSION

6.1 Self-gravitational vortex growth and hydrodynamic turbulence

Our main finding is that self-gravitating 3D vortices can survive the elliptic instability. Self-gravity enables vortex survival and growth even when the Toomre parameter $Q \sim 5$, which is significantly larger than that required for axisymmetric instability in 3D shearing boxes ($Q \lesssim 0.6$, Mamatashvili & Rice 2010). Thus the presence of a vortex reduces the gravitational stability of the flow.

We suggest that, provided the initial EI does not completely destroy the large-scale vortex flow topology (see §5.6 and §6.6), the vortex can then slowly grow under its self-gravity. (Without self-gravity the vortex always decays.) The growth spins up the vortex and its aspect-ratio decreases. This is expected for vortices in shearing discs, e.g. the GNG vortex spin increases with decreasing χ (see Eq. 16). Smaller aspect-ratio vortices favour EI (Lesur & Papaloizou 2009), which generates further hydrodynamic turbulence.

The vortex persists during secular growth because the subsequent EI is weak, as the vortex has been elongated by the initial EI. Our numerical experiments indicate a nec-

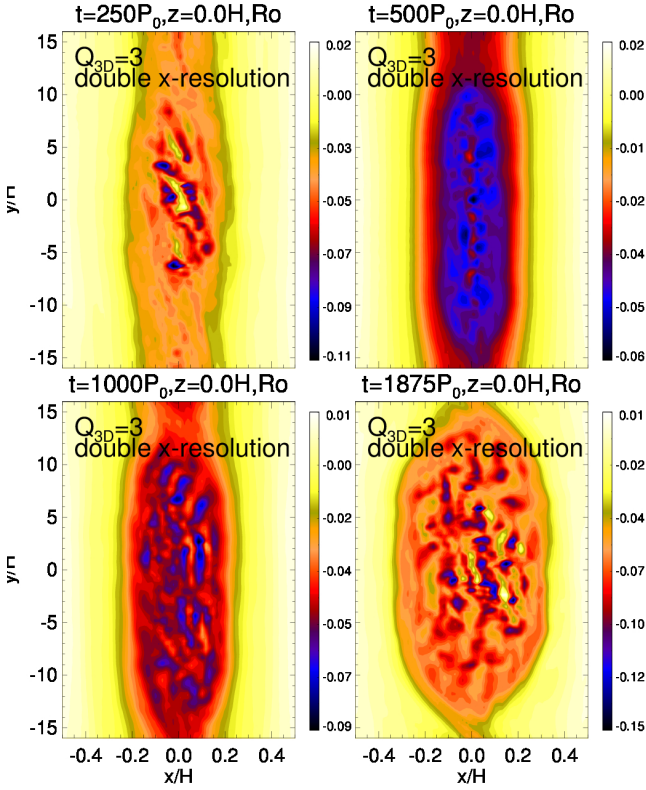


Figure 13. Vortex evolution in the $Q_{3D} = 3$ disc but with double the radial resolution than the fiducial runs.

essary condition for vortex survival is having gravitational stresses exceed Reynolds stresses ($\alpha_G \gtrsim \alpha_R$). It signifies the evolution being dominated by self-gravity with hydrodynamic turbulence being a byproduct.

To check that self-gravity can directly cause vortex growth, we ran several 2D simulations in Appendix C. We find for sufficiently strong self-gravity, the vortex can indeed grow without EI-induced turbulence. However, growth does not occur in razor-thin discs if $Q_{3D} \geq 4$, whereas we find growth in corresponding 3D simulations with EI. This suggests that EI-induced hydrodynamic turbulence may also contribute to gravitational instability, as discussed below.

6.2 Turbulence-enabled gravitational instability?

The EI converts the vortex's internal large-scale, planar rotation into small-scale 3D turbulence. However, removing rotation in a self-gravitating flow allows gravitational collapse. This type of gravitational instability rely on dissipative processes to remove rotational stabilization (Lynden-Bell & Pringle 1974). Comparing our 3D simulations that have EI and show vortex growth and supplementary 2D simulations in Appendix C that shows no EI or growth suggest that EI-turbulence may provide a similar effect; thus enabling vortex growth at large Q . This picture is similar to secular gravitational instabilities in viscous or dusty discs, whereby friction allow gravitational instabilities to develop even when $Q > 1$ (e.g. Schmit & Tscharnuter 1995; Taka-hashi & Inutsuka 2014).

Gravitational instability catalysed by EI-induced tur-

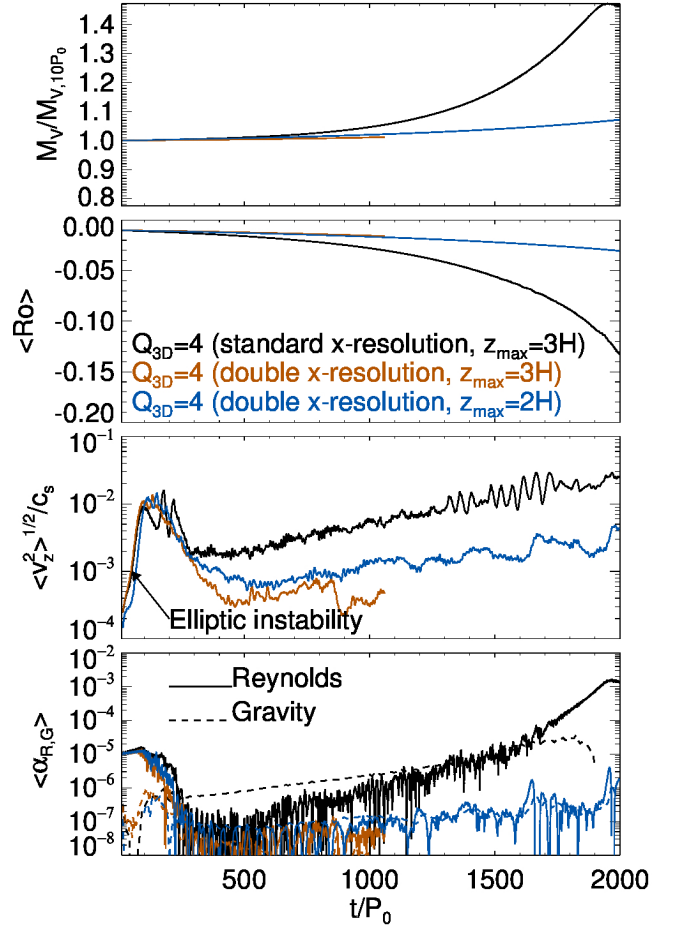


Figure 14. Vortex evolution in discs with $Q_{3D} = 4$ but different radial resolutions and vertical domain sizes.

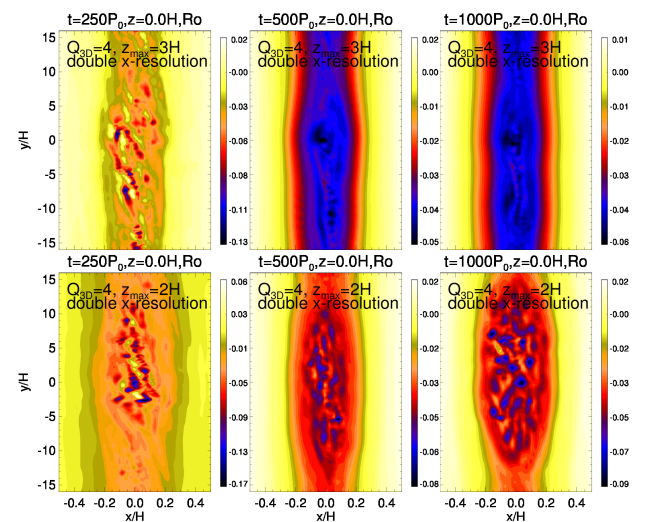


Figure 15. Effect of vertical domain size on vortex evolution. The disc has $Q_{3D} = 4$ and the simulations were performed with twice the fiducial radial resolution. The vortex does not survive with $z_{\max} = 3H$ but does with $z_{\max} = 2H$.

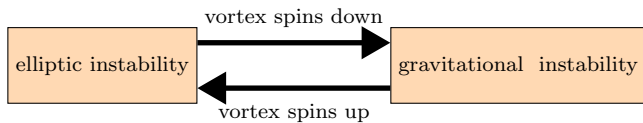


Figure 16. The ‘gravito-elliptic’ interpretation of the bursty behaviour observed towards the end of secular vortex growth. A vortex spins up and its aspect-ratio decreases, generating hydrodynamic turbulence via the EI. The associated turbulent viscosity favours gravitational instability by removing rotational support against self-gravity.

bulence leads to the possibility of ‘gravito-elliptic’ feedback, illustrated in Fig. 16. Vortex growth leads to hydrodynamic turbulence through the EI, which helps further collapse via secular gravitational instabilities, thus creating a cycle. The vortex attains a quasi-steady state if the destructive effect of EI is balanced by gravitational instability. This explains the ‘episodic bursts’ seen in our fiducial simulations when $\alpha_R \sim \alpha_G$ (§5.4).

6.3 Analogy with SBI in 3D

The episodic EI bursts observed in §5.4 bears some parallel to the Sub-critical Baroclinic Instability (SBI) in 3D. The SBI is a mechanism for amplifying vortices in non-isothermal discs and requires an unstable radial entropy gradient and an appropriate thermal diffusion or cooling timescale (Lesur & Papaloizou 2010). Neither are present in our standard, isothermal shearing boxes, Lesur & Papaloizou also found episodic EI in 3D simulations of the SBI.

In 3D, the SBI competes with the EI (Lesur & Papaloizou 2010; Lyra & Klahr 2011; Barge et al. 2016). These authors find the resulting vortex maintains its large-scale flow, but also contain small-scale, 3D hydrodynamic turbulence in its core. This is similar to our self-gravitating vortices (e.g. Fig. 8). Self-gravity plays the role of SBI in our simulations by amplifying the vortex.

The important difference is that for SBI there exists an explicit baroclinic vorticity source, which comes from the global radial entropy gradient. Self-gravity cannot directly source vorticity. However, the vortex can spin up as it collapses due to self-gravity. The result in both cases is that the vortex aspect-ratio decreases, feeding the EI, which tries to remove the large-scale vortex rotation.

6.4 Application to Rossby vortices

We can relate our simulations to vortex formation by the Rossby Wave Instability (RWI, Lovelace et al. 1999; Li et al. 2000, 2001). The RWI is a dynamical instability associated with radially-structured discs. More specifically, it requires a minimum in the disc’s potential vorticity profile ($= \omega/\Sigma$). Candidate sites include gap edges opened by planets (Lyra et al. 2009a; Li et al. 2009; Lin 2012a) and dead zone boundaries (Lyra et al. 2008, 2009b). These isolated radial structures often involve length scales of $O(H)$, and are thus consistent our typical vortex half-widths ($\lesssim H$).

The expected initial aspect ratio of Rossby vortices is $\chi = \pi/hm_{\max}$; here $m_{\max} \sim 5-8$ is the most unstable azimuthal wavenumber of the RWI (Lin & Papaloizou 2011b)

and $h = H/R$ is the disc aspect ratio. For protoplanetary discs with $h = 0.05-0.1$ we expect $\chi \sim 4-12$. Our nominal choice $\chi = 10$ is consistent with the lower bound on lower m_{\max} , which is applicable to thin and/or low mass discs (Lin & Papaloizou 2011b) as considered here. This is also the limit where Rossby vortices can merge. Thus our model could also correspond to a single, post-merger Rossby vortex.

6.5 Dust-trapping and observational implications

Our main result is that moderate disc self-gravity can help sustain 3D vortices in spite of the elliptic instability. This means that vortices are more likely to be observed in the outer parts of protoplanetary discs, where self-gravity becomes important. This could be relevant to vortex formation via the RWI due to gap-opening planets at large radii (Hammer et al. 2017) or the outer dead zone boundary (Lyra et al. 2015).

For definiteness, let us consider the class II circumstellar disc models described in Kratter & Lodato (2016, their Fig. 2a). For typical global accretion rates $\dot{M} \in [10^{-8}, 10^{-7}]M_{\odot}\text{yr}^{-1}$, the Toomre parameter ranges from $Q \simeq 10$ at 30AU to $Q \simeq 5$ at 100AU. These are similar to the Q values in our simulations. Furthermore, at these radii, heating is dominated by stellar irradiation (Chiang & Goldreich 1997) and thus disc behaves almost isothermally; also consistent with our equation of state. Note also our simulation timescales of $O(10^3)$ orbits corresponds 10^6 yrs at 100AU, which is of order the disc lifetime.

Our fiducial simulation ($Q_{3D} = 3$ or $Q \simeq 5$) corresponds to 100AU in this physical disc model. Although $Q > 2$ is traditionally considered non-self-gravitating (Kratter & Lodato 2016), neglecting self-gravity altogether would result in a weak vortex with vanishing over-density. However, properly including self-gravity gives a concentrated vortex (Fig. 9). This would suggest that the trapping of dust — often the observable — is favoured in self-gravitating discs.

On the other hand, self-gravitating 3D vortices have turbulent cores, which tends to expel dust particles due to turbulent dust diffusion (Youdin & Lithwick 2007). To examine this effect we use the dust-trapping model described in (Lyra & Lin 2013) assuming an underlying GNG vortex. They find the distribution of small, passive dust particles within the vortex core is given by

$$\rho_d(s) = \rho_{d,\max} \exp\left(-\frac{s^2}{2H_v^2}\right), \quad (36)$$

$$H_v \equiv \frac{H}{f(\chi)} \sqrt{\frac{\delta}{St + \delta}} \quad (37)$$

where $St = \Omega\tau_s$ is the Stokes number and τ_s is the stopping time characterizing dust-gas friction and δ is a dimensionless parameterization of turbulent dust diffusion. The GNG vortex has $f(\chi) \sim 0.7$ for $\chi \gg 1$ (see Lyra & Lin 2013, for details). Recall s is a co-ordinate that label elliptical streamlines in the vortex by their semi-minor axes (see §3).

We evaluate Eq. 37 using simulation results as input parameters. Assuming dust-gas interaction is dominated by drag forces, we set $\delta = \alpha_R$. We also use χ_p in place of χ , but this is immaterial since the function f is effectively constant for elongated vortices.

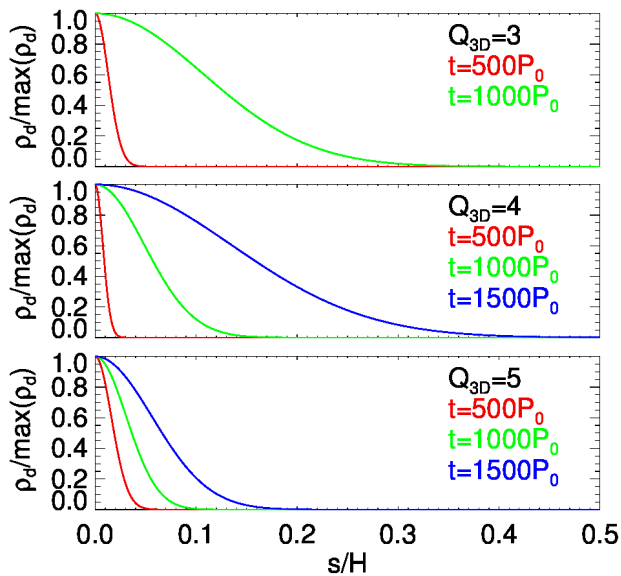


Figure 17. Normalised (mid-plane) dust density distribution obtained from the dust-trap model of Lyra & Lin (2013) with vortex parameters taken from the fiducial simulations. We fix the Stokes number $St = 10^{-3}$.

In Fig. 17 we plot the expected distribution of dust particles with $St = 10^{-3}$. We only consider the secular growth stage with EI turbulence occurring inside the vortex core, where Lyra & Lin’s model is applicable. In all cases dust is initially concentrated towards the centre, but over time it diffuses outward due to the increasing levels of hydrodynamic turbulence, which in turn is more vigorous with increasing self-gravity. Thus we can expect the dusty vortices to be wider in self-gravitating discs.

We comment that the above result for a single vortex may not be applicable to strongly self-gravitating discs with gravito-turbulence/fragmentation (Gammie 2001). However, in that limit it has also been shown that particle-trapping is enhanced by self-gravity (Gibbons et al. 2012, 2014, 2015; Shi et al. 2016).

6.6 Caveats and future directions

We have limited our study to classically stable discs, i.e. $Q > 2$ (or $Q_{3D} > 1$). It would be interesting to study 3D vortex evolution in strongly self-gravitating discs with $Q \lesssim 2$. However, in this limit the vortex must be initialised with care. Simply perturbing a strongly self-gravitating disc with the non-self-gravitating GNG vortex flow may result in transient effects. This problem may also be ill-posed because it is unclear if a single large-scale vortex can form in strongly self-gravitating discs in the first place. For example, it has been shown that the vortex-forming RWI can be suppressed by self-gravity (Lin & Papaloizou 2011b; Lovelace & Hohlfield 2013). Furthermore, classic gravitational instabilities can be expected in the ambient disc, which would complicate the evolution of an isolated vortex. We thus defer the strongly self-gravitating limit to a future study.

Returning to the $Q > 5$ discs considered in our study, the additional runs described in §5.6 indicate that 3D vor-

tices undergo secular self-gravitational growth only if the initial EI-induced turbulence does not destroy the large-scale vortex topology. In our simulations the initial EI turbulence strength is limited by a reduced vertical domain (Lithwick 2009) and/or numerical diffusion (Lesur & Papaloizou 2009). Since our models are inviscid, true numerical convergence may be difficult to achieve.

However, these effects may not be unrealistic. Numerical diffusion may mimic other sources of low-level turbulent viscosity in a protoplanetary disc (Umurhan et al. 2016a). Vortices can also be limited in vertical extent if the background disc has a layered structure (Bai 2016). The presence of an active vortex-driving source may also help to retain the large-scale vortex flow against the initial EI. Nevertheless, future works should incorporate these physical effects explicitly.

Local shearing box simulations do not permit a proper study of vortex gap-opening and migration (Paardekooper et al. 2010), which stem from global spiral density waves launched by the vortex. Clearly, one must eventually perform global disc simulations of self-gravitating 3D vortices. This is computationally challenging because of the need to simultaneously resolve the small-scale elliptic instability. Though some recent non-self-gravitating, global simulations have done so (Richard et al. 2016; Barge et al. 2016), including 3D self-gravity can significantly increase the computational cost.

However, our simulations show that even with EI-induced hydrodynamic turbulence, the vortex maintains a smooth density field with moderate amplitude. Furthermore, elongated vortices do not require high resolution in azimuth. This means that an accurate global Poisson solver (with sub- H resolution) is not essential for this problem.

We have purposefully neglected vortex-forming mechanisms to isolate the effect of self-gravity on vortex evolution. Nevertheless, future work should account for hydrodynamic instabilities that drive vortex formation (RWI, ConO/SBI, ZVI, or VSI), which require improved geometries and physics such as cooling.

Finally, we performed pure gas simulations and only estimated the extent of vortex dust-trapping in post-processing. It will be desirable to conduct two-phase, gas-dust simulations to properly capture the evolution of dust particles and the back reaction of drag forces on the gas. The latter becomes important for high dust-to-gas ratios, which can be expected in vortex centres (Fu et al. 2014; Crnkovic-Rubsamen et al. 2015; Surville et al. 2016). A simple starting point to model these effects is the one-fluid, thermodynamic model of dusty gas recently developed by Lin & Youdin (2017).

7 SUMMARY

In this paper we study the evolution of 3D vortices in self-gravitating protoplanetary discs via customised numerical simulations in the shearing box framework. We find self-gravity can help 3D vortices survive against elliptic instabilities that would otherwise destroy them in non-self-gravitating discs. With moderate self-gravity the result is a 3D vortex with a turbulent core. We emphasize that our disc models are gravitationally stable in the traditional sense

that Toomre Q values safely exceed unity; yet we observe vortex growth, albeit on timescales of $O(10^3)$ orbits. This indicates that the presence of a vortex reduces the long-term stability of the flow.

In addition to hydrodynamic turbulence as a byproduct of self-gravitational vortex growth via elliptic instabilities, we suggest secular gravitational instabilities can be catalysed by the hydrodynamic turbulence that result from the elliptic instability. The elliptic instability removes rotational support against self-gravity, which favours gravitational instability; but the subsequent spin-up of the vortex feeds the elliptic instability. There is competition between the vortex destruction by the elliptic instability and vortex growth due to self-gravity (either directly or assisted by hydrodynamic turbulence); thus a quasi-steady state is possible. Our simulations suggest vortices survive more easily, and hence are more likely observed, in protoplanetary discs at large radii.

ACKNOWLEDGMENTS

We thank the anonymous referee for a detailed report that lead to an improved physical interpretation and presentation of our results. This work is supported by the Theoretical Institute for Advanced Research in Astrophysics (TIARA) based in Academia Sinica Institute of Astronomy and Astrophysics (ASIAA). All 3D simulations were performed on the TIARA High Performance Computing cluster. The early stages of this project was carried out at the University of Arizona under the support of the Steward Theory Fellowship and made use of the El Gato and Ocelote clusters. This work is also part of the NASA Astrophysics Theory Program NNX17AK59G. Computer time for the 2D runs presented in this paper was provided by HPC resources of Cines under allocation A0010406957 made by GENCI (Grand Equipement National de Calcul Intensif).

REFERENCES

- Adams F. C., Watkins R., 1995, *ApJ*, **451**, 314
- Bai X.-N., 2016, *ApJ*, **821**, 80
- Barge P., Sommeria J., 1995, *A&A*, **295**, L1
- Barge P., Richard S., Le Dizès S., 2016, *A&A*, **592**, A136
- Barker A. J., Latter H. N., 2015, *MNRAS*, **450**, 21
- Bodo G., Chagelishvili G., Murante G., Tevzadze A., Rossi P., Ferrari A., 2005, *A&A*, **437**, 9
- Bodo G., Tevzadze A., Chagelishvili G., Mignone A., Rossi P., Ferrari A., 2007, *A&A*, **475**, 51
- Casassus S., et al., 2013, *Nature*, **493**, 191
- Chandrasekhar S., 1969, Ellipsoidal figures of equilibrium
- Chang P., Oishi J. S., 2010, *ApJ*, **721**, 1593
- Chiang E. I., Goldreich P., 1997, *ApJ*, **490**, 368
- Crida A., Morbidelli A., Masset F., 2006, *Icarus*, **181**, 587
- Crnkovic-Rubsamen I., Zhu Z., Stone J. M., 2015, *MNRAS*, **450**, 4285
- Dong R., Li S., Chiang E., Li H., 2017, *ApJ*, **843**, 127
- Fu W., Li H., Lubow S., Li S., 2014, *ApJ*, **788**, L41
- Fukagawa M., et al., 2013, *PASJ*, **65**, L14
- Gammie C. F., 2001, *ApJ*, **553**, 174
- Gibbons P. G., Rice W. K. M., Mamatsashvili G. R., 2012, *MNRAS*, **426**, 1444
- Gibbons P. G., Mamatsashvili G. R., Rice W. K. M., 2014, *MNRAS*, **442**, 361
- Gibbons P. G., Mamatsashvili G. R., Rice W. K. M., 2015, *MNRAS*, **453**, 4232
- Godon P., Livio M., 1999, *ApJ*, **523**, 350
- Goldreich P., Lynden-Bell D., 1965, *MNRAS*, **130**, 125
- Goodman J., Narayan R., Goldreich P., 1987, *MNRAS*, **225**, 695
- Hammer M., Kratter K. M., Lin M.-K., 2017, *MNRAS*, **466**, 3533
- Hashimoto J., et al., 2015, *ApJ*, **799**, 43
- Heinemann T., Papaloizou J. C. B., 2009, *MNRAS*, **397**, 52
- Inaba S., Barge P., 2006, *ApJ*, **649**, 415
- Isella A., Pérez L. M., Carpenter J. M., Ricci L., Andrews S., Rosenfeld K., 2013, *ApJ*, **775**, 30
- Johnson B. M., Gammie C. F., 2005, *ApJ*, **635**, 149
- Kerswell R. R., 1994, *Journal of Fluid Mechanics*, **274**, 219
- Kida S., 1981, *Journal of the Physical Society of Japan*, **50**, 3517
- Klahr H., Hubbard A., 2014, *ApJ*, **788**, 21
- Kraichnan R. H., Montgomery D., 1980, *Reports on Progress in Physics*, **43**, 547
- Kratter K., Lodato G., 2016, *ARA&A*, **54**, 271
- Kraus S., et al., 2017, *ApJ*, **848**, L11
- Latter H. N., 2016, *MNRAS*, **455**, 2608
- Lesur G. R. J., Latter H., 2016, *MNRAS*, **462**, 4549
- Lesur G., Papaloizou J. C. B., 2009, *A&A*, **498**, 1
- Lesur G., Papaloizou J. C. B., 2010, *A&A*, **513**, A60
- Li H., Finn J. M., Lovelace R. V. E., Colgate S. A., 2000, *ApJ*, **533**, 1023
- Li H., Colgate S. A., Wendroff B., Liska R., 2001, *ApJ*, **551**, 874
- Li H., Lubow S. H., Li S., Lin D. N. C., 2009, *ApJ*, **690**, L52
- Lin M.-K., 2012a, *MNRAS*, **426**, 3211
- Lin M.-K., 2012b, *ApJ*, **754**, 21
- Lin M.-K., Kratter K. M., 2016, *ApJ*, **824**, 91
- Lin M.-K., Papaloizou J. C. B., 2011a, *MNRAS*, pp 876+
- Lin M.-K., Papaloizou J. C. B., 2011b, *MNRAS*, **415**, 1426
- Lin M.-K., Youdin A. N., 2015, *ApJ*, **811**, 17
- Lin M.-K., Youdin A. N., 2017, *ApJ*, **849**, 129
- Lithwick Y., 2007, *ApJ*, **670**, 789
- Lithwick Y., 2009, *ApJ*, **693**, 85
- Lovelace R. V. E., Hohlfeld R. G., 2013, *MNRAS*, **429**, 529
- Lovelace R. V. E., Li H., Colgate S. A., Nelson A. F., 1999, *ApJ*, **513**, 805
- Lynden-Bell D., Pringle J. E., 1974, *MNRAS*, **168**, 603
- Lyra W., 2014, *ApJ*, **789**, 77
- Lyra W., Klahr H., 2011, *A&A*, **527**, A138+
- Lyra W., Lin M.-K., 2013, *ApJ*, **775**, 17
- Lyra W., Johansen A., Klahr H., Piskunov N., 2008, *A&A*, **491**, L41
- Lyra W., Johansen A., Klahr H., Piskunov N., 2009a, *A&A*, **493**, 1125
- Lyra W., Johansen A., Zsom A., Klahr H., Piskunov N., 2009b, *A&A*, **497**, 869
- Lyra W., Turner N. J., McNally C. P., 2015, *A&A*, **574**, A10
- Mamatsashvili G. R., Chagelishvili G. D., 2007, *MNRAS*, **381**, 809
- Mamatsashvili G. R., Rice W. K. M., 2009, *MNRAS*, **394**, 2153
- Mamatsashvili G. R., Rice W. K. M., 2010, *MNRAS*, **406**, 2050
- Marcus P. S., Pei S., Jiang C.-H., Barranco J. A., Hassanzadeh P., Lecoanet D., 2015, *ApJ*, **808**, 87
- Marino S., Casassus S., Perez S., Lyra W., Roman P. E., Avenhaus H., Wright C. M., Maddison S. T., 2015, *ApJ*, **813**, 76
- Meheut H., Casse F., Varniere P., Tagger M., 2010, *A&A*, **516**, A31+
- Meheut H., Meliani Z., Varniere P., Benz W., 2012, *A&A*, **545**, A134
- Nelson R. P., Gressel O., Umurhan O. M., 2013, *MNRAS*, **435**, 2610
- Ohta Y., et al., 2016, *PASJ*, **68**, 53
- Ono T., Muto T., Takeuchi T., Nomura H., 2016, *ApJ*, **823**, 84
- Paardekooper S., Lesur G., Papaloizou J. C. B., 2010, *ApJ*, **725**, 146

- Pérez L. M., Isella A., Carpenter J. M., Chandler C. J., 2014, *ApJ*, **783**, L13
- Petersen M. R., Julien K., Stewart G. R., 2007, *ApJ*, **658**, 1236
- Raettig N., Lyra W., Klahr H., 2013, *ApJ*, **765**, 115
- Railton A. D., Papaloizou J. C. B., 2014, *MNRAS*, **445**, 4409
- Regály Z., Vorobyov E., 2017, *MNRAS*, **471**, 2204
- Richard S., Nelson R. P., Umurhan O. M., 2016, *MNRAS*, **456**, 3571
- Schmit U., Tscharnuter W. M., 1995, *Icarus*, **115**, 304
- Shen Y., Stone J. M., Gardiner T. A., 2006, *ApJ*, **653**, 513
- Shi J.-M., Zhu Z., Stone J. M., Chiang E., 2016, *MNRAS*, **459**, 982
- Stoll M. H. R., Kley W., 2014, *A&A*, **572**, A77
- Stone J. M., Gardiner T. A., 2010, *ApJS*, **189**, 142
- Stone J. M., Gardiner T. A., Teuben P., Hawley J. F., Simon J. B., 2008, *ApJS*, **178**, 137
- Surville C., Mayer L., Lin D. N. C., 2016, *ApJ*, **831**, 82
- Takahashi S. Z., Inutsuka S.-i., 2014, *ApJ*, **794**, 55
- Toomre A., 1964, *ApJ*, **139**, 1217
- Umurhan O. M., Regev O., 2004, *A&A*, **427**, 855
- Umurhan O. M., Estrada R. R., Cuzzi J. N., 2016a, in *Lunar and Planetary Science Conference*. p. 2887
- Umurhan O. M., Shariff K., Cuzzi J. N., 2016b, *ApJ*, **830**, 95
- Yellin-Bergovoy R., Heifetz E., Umurhan O. M., 2016, *Geophysical and Astrophysical Fluid Dynamics*, **110**, 274
- Youdin A. N., 2011, *ApJ*, **731**, 99
- Youdin A. N., Lithwick Y., 2007, *Icarus*, **192**, 588
- Zhu Z., Baruteau C., 2016, *MNRAS*, **458**, 3918
- Zhu Z., Stone J. M., Rafikov R. R., 2013, *ApJ*, **768**, 143
- Zhu Z., Stone J. M., Rafikov R. R., Bai X.-n., 2014, *ApJ*, **785**, 122
- Zhu Z., Ju W., Stone J. M., 2016, *ApJ*, **832**, 193
- van der Marel N., et al., 2013, *Science*, **340**, 1199
- van der Marel N., Cazzoletti P., Pinilla P., Garufi A., 2016, *ApJ*, **832**, 178

APPENDIX A: SHEARING BOX EQUATIONS IN ELLIPTICO-POLAR CO-ORDINATES

In elliptico-polar co-ordinates (s, φ, z) the divergence and advective derivative operators have identical form to that in the usual cylindrical co-ordinates. That is,

$$\nabla \cdot \mathbf{W} = \frac{1}{s} \frac{\partial}{\partial s} (sW_s) + \frac{1}{s} \frac{\partial W_\varphi}{\partial \varphi} + \frac{\partial W_z}{\partial z}, \quad (\text{A1})$$

$$\mathbf{W} \cdot \nabla = W_s \frac{\partial}{\partial s} + \frac{W_\varphi}{s} \frac{\partial}{\partial \varphi} + W_z \frac{\partial}{\partial z}, \quad (\text{A2})$$

for any vector field \mathbf{W} . The continuity equation thus retain the same form as in the Cartesian box, as does the vertical momentum equation. The horizontal momentum equations, however, are modified to read

$$\begin{aligned} \frac{\partial v_s}{\partial t} + \mathbf{v} \cdot \nabla v_s - \frac{v_\varphi^2}{s} \\ = \frac{1}{2} (\xi_+ + \xi_- \cos 2\varphi) \left(2\Omega\chi v_\varphi - \frac{\partial \eta}{\partial s} \right) \\ + \frac{\xi_-}{2} \sin 2\varphi \left(2\Omega\chi v_s + \frac{1}{s} \frac{\partial \eta}{\partial \varphi} \right) + q\Omega^2 s (\cos 2\varphi + 1) \end{aligned} \quad (\text{A3})$$

$$\begin{aligned} \frac{\partial v_\varphi}{\partial t} + \mathbf{v} \cdot \nabla v_\varphi + \frac{v_\varphi v_s}{s} \\ = \frac{\xi_-}{2} \sin 2\varphi \left(\frac{\partial \eta}{\partial s} - 2\Omega\chi v_\varphi \right) \\ - \frac{1}{2} (\xi_+ - \xi_- \cos 2\varphi) \left(\frac{1}{s} \frac{\partial \eta}{\partial \varphi} + 2\Omega\chi v_s \right) - q\Omega^2 s \sin 2\varphi, \end{aligned} \quad (\text{A4})$$

where

$$\xi_\pm = 1 \pm \frac{1}{\chi^2}. \quad (\text{A5})$$

Finally, the Poisson equation becomes

$$\begin{aligned} \left[\frac{1}{2} (\xi_- \cos 2\varphi + \xi_+) \frac{\partial^2}{\partial s^2} + \frac{1}{2s^2} (\xi_+ - \xi_- \cos 2\varphi) \frac{\partial^2}{\partial \varphi^2} \right. \\ \left. - \frac{\xi_-}{s} \sin 2\varphi \frac{\partial^2}{\partial \varphi \partial s} + \frac{1}{2s} (\xi_+ - \xi_- \cos 2\varphi) \frac{\partial}{\partial s} + \frac{\xi_-}{s^2} \sin 2\varphi \frac{\partial}{\partial \varphi} \right. \\ \left. + \frac{\partial^2}{\partial z^2} \right] \Phi = 4\pi G\rho. \end{aligned} \quad (\text{A6})$$

APPENDIX B: LINEAR RESPONSE OF THE GNG VORTEX TO ITS GRAVITATIONAL POTENTIAL

We explore the perturbative effect of introducing self-gravity on the GNG vortex solution. We simplify the problem by considering an unstratified disc with no vertical velocities. Then $v_z = \partial_z = 0$. This should be an adequate approximation for regions close to the vortex centre $(s, z \rightarrow 0)$. We set

$$G \rightarrow 0 + \delta G. \quad (\text{B1})$$

This induces perturbations

$$\rho \rightarrow \rho(s) + \delta\rho, \quad (\text{B2})$$

$$v_s \rightarrow 0 + \delta v_s, \quad (\text{B3})$$

$$v_\varphi \rightarrow -\Omega_v s + \delta v_\varphi, \quad (\text{B4})$$

$$\Phi \rightarrow 0 + \delta\Phi. \quad (\text{B5})$$

The background flow, $v_\varphi(s)$ and $\rho(s)$, is given by the non-self-gravitating GNG vortex solution (Eq. 16–17) with the vertical dimension suppressed. Since the basic state is symmetric in φ , we Fourier analyse in azimuth and write

$$\begin{bmatrix} \delta\rho \\ \delta v_s \\ \delta v_\varphi \\ \delta\Phi \end{bmatrix} = \text{Re} \sum_{l=0}^{\infty} \begin{bmatrix} \rho Q_l / c_s^2 \\ iU_l \\ V_l \\ \Phi_l \end{bmatrix} \exp il\varphi. \quad (\text{B6})$$

We insert the above perturbations into the steady state continuity, horizontal momentum and Poisson equations and linearize. We then multiply by $e^{-in\varphi}$, and integrate in φ to obtain

$$\frac{1}{s} (s\rho U_n)' + \frac{n}{s} \rho V_n - n\Omega_v \frac{\rho Q_n}{c_s^2} = 0 \quad (\text{B7})$$

$$\quad (\text{B8})$$

from the continuity equation, where $'$ denotes d/ds ; and the

horizontal momentum equations give

$$\begin{aligned}
2\Omega_v V_n + n\Omega_v U_n = & -\frac{1}{2} \left[\xi_+ \tilde{\eta}'_n + \frac{\xi_-}{2} (\tilde{\eta}'_{n-2} + \tilde{\eta}'_{n+2}) \right] \\
& + \frac{\xi_-}{4s} [(n-2)\tilde{\eta}_{n-2} - (n+2)\tilde{\eta}_{n+2}] \\
& + \frac{1}{2} \Omega \xi_- \chi (U_{n-2} - U_{n+2}) \\
& + \Omega \chi \left[\xi_+ V_n + \frac{\xi_-}{2} (V_{n-2} + V_{n+2}) \right], \tag{B9}
\end{aligned}$$

$$\begin{aligned}
2\Omega_v U_n + n\Omega_v V_n = & \frac{\xi_-}{4} (\tilde{\eta}'_{n-2} - \tilde{\eta}'_{n+2}) \\
& + \frac{1}{2s} \left\{ n\xi_+ \tilde{\eta}_n \right. \\
& \quad \left. - \frac{\xi_-}{2} [(n-2)\tilde{\eta}_{n-2} + (n+2)\tilde{\eta}_{n+2}] \right\} \\
& - \frac{1}{2} \Omega \xi_- \chi (V_{n-2} - V_{n+2}) \\
& + \Omega \chi \left[\xi_+ U_n - \frac{\xi_-}{2} (U_{n-2} + U_{n+2}) \right], \tag{B10}
\end{aligned}$$

where

$$\tilde{\eta}_n \equiv \mathcal{Q}_n + \Phi_n. \tag{B11}$$

Adding and subtracting the horizontal momentum equations gives the more compact form

$$\begin{aligned}
\frac{\xi_+}{2} \left(\tilde{\eta}'_n + \frac{n}{s} \tilde{\eta}_n \right) + \frac{\xi_-}{2} \left(\tilde{\eta}'_{n-2} - \frac{n-2}{s} \tilde{\eta}_{n-2} \right) \\
= [(2-n)\Omega_v - \Omega \chi \xi_+] Y_n + \Omega \chi \xi_- X_{n-2}, \\
\frac{\xi_+}{2} \left(\tilde{\eta}'_n - \frac{n}{s} \tilde{\eta}_n \right) + \frac{\xi_-}{2} \left(\tilde{\eta}'_{n+2} + \frac{n+2}{s} \tilde{\eta}_{n+2} \right) \\
= [\Omega \chi \xi_+ - (n+2)\Omega_v] X_n - \Omega \chi \xi_- Y_{n+2}, \tag{B12}
\end{aligned}$$

where

$$X_n \equiv U_n + V_n, \tag{B13}$$

$$Y_n \equiv U_n - V_n. \tag{B14}$$

The linearized Poisson equation is

$$\begin{aligned}
\frac{\xi_-}{4} \left[\frac{d^2}{ds^2} - \frac{(2n-3)}{s} \frac{d}{ds} + \frac{n(n-2)}{s^2} \right] \Phi_{n-2} \\
+ \frac{\xi_+}{2} \left(\frac{d^2}{ds^2} + \frac{1}{s} \frac{d}{ds} - \frac{n^2}{s^2} \right) \Phi_n \\
+ \frac{\xi_-}{4} \left[\frac{d^2}{ds^2} + \frac{(2n+3)}{s} \frac{d}{ds} + \frac{n(n+2)}{s^2} \right] \Phi_{n+2} \\
= 4\pi \delta G \rho(s) \delta_{n0}. \tag{B15}
\end{aligned}$$

B1 The $n = 2$ problem

To make analytic progress we truncate the series expansion (Eq. B6) at $n = 2$. Then for $n = 0$ we have

$$\frac{\xi_+}{2} \tilde{\eta}'_0 = (\Omega \chi \xi_+ - 2\Omega_v) V_0, \tag{B16}$$

$$\frac{\xi_+}{2} \tilde{\eta}'_0 + \frac{\xi_-}{2} \left(\tilde{\eta}'_2 + \frac{2}{s} \tilde{\eta}_2 \right) = (\Omega \chi \xi_+ - 2\Omega_v) V_0 - \Omega \chi \xi_- Y_2, \tag{B17}$$

where we have utilized the fact that $U_0 = 0$ as implied by the continuity equation (Eq. B7) for $n = 0$. Next, for $n = 2$ we have

$$\frac{\xi_+}{2} \left(\tilde{\eta}'_2 + \frac{2}{s} \tilde{\eta}_2 \right) + \frac{\xi_-}{2} \tilde{\eta}'_0 = \Omega \chi \xi_- V_0 - \Omega \chi \xi_+ Y_2, \tag{B18}$$

$$\frac{\xi_+}{2} \left(\tilde{\eta}'_2 - \frac{2}{s} \tilde{\eta}_2 \right) = (\Omega \chi \xi_+ - 4\Omega_v) X_2. \tag{B19}$$

Eq. B16–B19 imply

$$\tilde{\eta}'_0 = V_0 = 0, \tag{B20}$$

$$2\Omega_v V_2 = \frac{\xi_\pm}{s} \tilde{\eta}_2 + (\Omega \chi \xi_+ - 2\Omega_v) U_2, \tag{B21}$$

Hence, an ODE for $\tilde{\eta}_2$ is

$$\tilde{\eta}'_2 + \frac{1}{s} \left(2 - \frac{\Omega \chi \xi_+}{\Omega_v} \right) \tilde{\eta}_2 + \Omega \chi \left(4 - \frac{\Omega \chi \xi_+}{\Omega_v} \right) U_2 = 0. \tag{B22}$$

Next, the $n = 2$ continuity equation, after using Eq. B11 and B21, becomes

$$\begin{aligned}
U'_2 + \left[\frac{\rho'}{\rho} + \frac{1}{s} \left(\frac{\Omega \chi \xi_+}{\Omega_v} - 1 \right) \right] U_2 + \left(\frac{\xi_+}{s^2 \Omega_v} - \frac{2\Omega_v}{c_s^2} \right) \tilde{\eta}_2 \\
+ \frac{2\Omega_v}{c_s^2} \Phi_2 = 0. \tag{B23}
\end{aligned}$$

Further eliminating U_2 gives a second order ODE for $\tilde{\eta}_2$:

$$\begin{aligned}
\tilde{\eta}''_2 + \left(\frac{\rho'}{\rho} + \frac{1}{s} \right) \tilde{\eta}'_2 + \left[\frac{\lambda \rho'}{s \rho} + 2\Omega \chi (\lambda + 2) \frac{\Omega_v}{c_s^2} - \frac{4}{s^2} \right] \tilde{\eta}_2 \\
= 2\Omega \chi (\lambda + 2) \frac{\Omega_v}{c_s^2} \Phi_2, \tag{B24}
\end{aligned}$$

where $\lambda \equiv 2 - \Omega \chi \xi_+ / \Omega_v$. We require $\tilde{\eta}'_2(0) = \tilde{\eta}_2(0) = 0$.

Eq. B24 describes the non-axisymmetric response of the GNG vortex to the potential Φ_2 . We are interested in the case where the potential arises from the vortex mass itself. Thus Φ_2 is given by a solution to the linearized Poisson solution.

B2 Approximate solution as $s \rightarrow 0$

Here we consider the approximate solution to Eq. B24 for small s . We first obtain the potential solution Φ_2 . To do so in a tractable manner, we apply the ‘source term approximation’ to solve the Poisson equation as follows.

We first solve the $n = 0$ cylindrical Poisson equation neglecting the $n = 2$ term,

$$\Phi''_0 + \frac{1}{s} \Phi'_0 = \frac{2\Omega^2}{\xi_+ Q_{3D}} \exp(-s^2/2H_{\text{eff}}^2). \tag{B25}$$

The solution is

$$\Phi'_0 = \frac{2\Omega^2 H_{\text{eff}}^2}{\xi_+ Q_{3D} s} \frac{1}{s} [1 - \exp(-s^2/2H_{\text{eff}}^2)]. \tag{B26}$$

We then use the above solution for Φ'_0 as a source term in the $n = 2$ Poisson equation

$$\begin{aligned}
\Phi''_2 + \frac{1}{s} \Phi'_2 - \frac{4}{s^2} \Phi_2 = -\frac{\xi_-}{2\xi_+} \left(\Phi''_0 - \frac{1}{s} \Phi'_0 \right) \\
\approx \frac{\xi_- \Omega^2}{4\xi_+^2 Q_{3D} H_{\text{eff}}^2} s^2 \equiv A s^2, \tag{B27}
\end{aligned}$$

where for the approximation we have expanded the solution

for Φ'_0 to first order in $s^2/2H_{\text{eff}}^2$. The approximate solution for Φ_2 is then

$$\Phi_2 \simeq \frac{\mathcal{A}}{12} s^4. \quad (\text{B28})$$

For small s Eq. B24, with the above solution for Φ_2 , is approximately

$$\tilde{\eta}_2'' + \frac{1}{s} \tilde{\eta}_2' - \frac{4}{s^2} \tilde{\eta}_2 = \mathcal{B} s^4, \quad (\text{B29})$$

where

$$\mathcal{B} \equiv \mathcal{A} \Omega \chi (\lambda + 2) \Omega_v / 6c_s^2. \quad (\text{B30})$$

The solution is

$$\tilde{\eta}_2 = \frac{\mathcal{B} s^6}{32}. \quad (\text{B31})$$

The corresponding solution for U_2 and V_2 can be obtained from Eq. B23 and B21, respectively. We find

$$U_2 = -\frac{\mathcal{A} \Omega_v}{192c_s^2} (6 + \lambda) s^5, \quad (\text{B32})$$

and

$$V_2 - U_2 = \frac{\mathcal{A} \Omega_v}{48c_s^2} (2 + \lambda) s^5. \quad (\text{B33})$$

B3 Vorticity perturbation

The perturbation to the vertical component of vorticity, $\delta\omega$, is defined in Cartesian co-ordinates as

$$\delta\omega \equiv \frac{\partial}{\partial x} \delta v_y - \frac{\partial}{\partial y} \delta v_x. \quad (\text{B34})$$

Expanding $\delta\omega$ similarly to Eq. B6 and written in terms of the perturbed elliptico-polar velocity components U_n, V_n we have

$$\begin{aligned} \omega_n = & \frac{\chi \xi_+}{2} V_n' + \frac{\chi \xi_+}{2s} (V_n + nU_n) \\ & + \frac{\chi \xi_-}{4} \left(\frac{d}{ds} - \frac{n-1}{s} \right) (U_{n-2} + V_{n-2}) \\ & - \frac{\chi \xi_-}{4} \left(\frac{d}{ds} + \frac{n+1}{s} \right) (U_{n+2} - V_{n+2}). \end{aligned} \quad (\text{B35})$$

Then

$$\omega_0 = \frac{\chi \xi_-}{4} \left(\frac{d}{ds} + \frac{1}{s} \right) (V_2 - U_2). \quad (\text{B36})$$

Inserting the above solution for small s , Eq. B33, we find

$$\omega_0 = \frac{\xi_-^2 \chi}{128 \xi_+^2 Q_{3D} F^2} (4\Omega_v - \Omega \chi \xi_+) \left(\frac{s}{H_{\text{eff}}} \right)^4. \quad (\text{B37})$$

Because of the second term in brackets, the sign of the vorticity perturbation depends on χ . For $\chi \gtrsim 2.56$ the vorticity is made more negative by self-gravity and vice versa.

APPENDIX C: VORTEX EVOLUTION IN 2D DISCS

We also simulated vortex evolution in 2D, razor-thin self-gravitating discs. These simulations were carried out in global cylindrical geometry (R, ϕ) using the GENESIS code in a setup similar to Pierens & Lin (submitted). However,

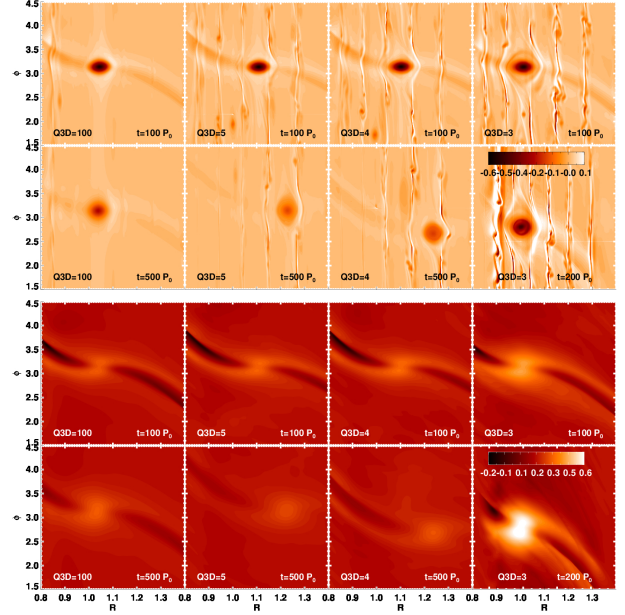


Figure C1. Razor-thin, 2D global self-gravitating disc simulations of vortex evolution. Top: Rossby number; bottom: surface density.

we adopt the same self-gravity parameter and vortex initialization as in our 3D simulations.

Fig. C1 compares the vortex evolution in discs with $Q_{3D} = 3, 4, 5$ and 100. Being 2D, the elliptic instability is suppressed and thus plays no role in these simulations. The $Q_{3D} = 100$ vortex decays due to numerical diffusion. This also occurs for the $Q_{3D} = 4, 5$, unlike in the corresponding 3D fiducial simulations where we find secular growth. The $Q_{3D} = 3$ case does show vortex growth, similar to the corresponding 3D simulation.

In Fig. C2 we plot the time evolution of vortex properties in the $Q_{3D} = 3$, 2D disc. Similar to the 3D case, vortex growth is limited to $\lesssim H$ in its half-width. The global setup here allows us to simulate beyond this stage without interference from boundary conditions. We find the vortex induces strong spiral shocks and is weakened, signified by the drop in $|\text{Ro}|$. The vortex is eventually destroyed by $t = 500P_0$, i.e. it does not readjust into a new configuration (Bodo et al. 2007). This self-limited growth is qualitatively similar to Mamatsashvili & Rice (2009). However, Mamatsashvili & Rice (2009) considered non-isothermal discs with Q of order unity, which results in a gravito-turbulent state with multiple vortices, each lasting only two orbits; whereas our isolated vortex persists for ~ 300 orbits.

For the $Q_{3D} = 3$, 2D disc we also experimented with different parameters, including the disc aspect-ratio and flaring index, surface density profile, and the initial vortex perturbation aspect-ratio. The results are shown in Fig. C3. We find vortex growth is robust, unless the vortex is initially weak (left panel). This supports the idea that a sufficiently strong vortex reduces the local gravitational stability of the disc.

Comparing these 2D simulations to our 3D cases indicate that for small Q_{3D} (e.g. 3) EI-turbulence is not necessary for the vortex to undergo self-gravitational growth.

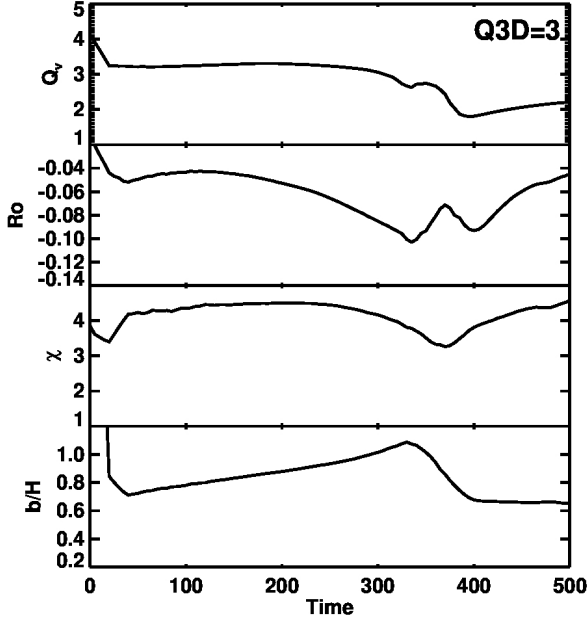


Figure C2. Vortex evolution in the razor-thin, 2D disc with $Q_{3D} = 3$ shown in Fig. C1. Top to bottom: Toomre Q at the vortex centre, Rossby number, aspect-ratio, and radial size.

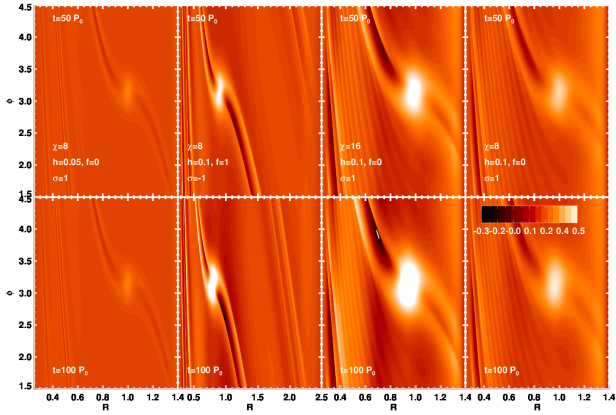


Figure C3. Razor-thin, 2D global self-gravitating disc simulations of vortex evolution. We fix $Q_{3D} = 3$ but use different aspect-ratios h and flaring indices $f \equiv \partial \ln h / \partial \ln R$, surface density profiles $\sigma \equiv -\partial \ln \Sigma / \partial \ln R$, and the initial vortex aspect-ratios χ .

However, at larger Q_{3D} , self-gravity in itself is insufficient for vortex growth. Instead, we suggest for $Q_{3D} \gtrsim 3$, EI-turbulence can mediate vortex growth via secular gravitational instabilities, since for $Q_{3D} = 4, 5$ we only observe growth in the 3D simulations with EI, and not in the laminar, 2D discs.